

High-Fidelity Generalization Method of Cells for Inelastic Periodic Multiphase Materials

Jacob Aboudi
Tel-Aviv University, Ramat-Aviv, Israel

Marek-Jerzy Pindera
University of Virginia, Charlottesville, Virginia

Steven M. Arnold
Glenn Research Center, Cleveland, Ohio

The NASA STI Program Office . . . in Profile

Since its founding, NASA has been dedicated to the advancement of aeronautics and space science. The NASA Scientific and Technical Information (STI) Program Office plays a key part in helping NASA maintain this important role.

The NASA STI Program Office is operated by Langley Research Center, the Lead Center for NASA's scientific and technical information. The NASA STI Program Office provides access to the NASA STI Database, the largest collection of aeronautical and space science STI in the world. The Program Office is also NASA's institutional mechanism for disseminating the results of its research and development activities. These results are published by NASA in the NASA STI Report Series, which includes the following report types:

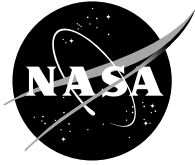
- **TECHNICAL PUBLICATION.** Reports of completed research or a major significant phase of research that present the results of NASA programs and include extensive data or theoretical analysis. Includes compilations of significant scientific and technical data and information deemed to be of continuing reference value. NASA's counterpart of peer-reviewed formal professional papers but has less stringent limitations on manuscript length and extent of graphic presentations.
- **TECHNICAL MEMORANDUM.** Scientific and technical findings that are preliminary or of specialized interest, e.g., quick release reports, working papers, and bibliographies that contain minimal annotation. Does not contain extensive analysis.
- **CONTRACTOR REPORT.** Scientific and technical findings by NASA-sponsored contractors and grantees.

- **CONFERENCE PUBLICATION.** Collected papers from scientific and technical conferences, symposia, seminars, or other meetings sponsored or cosponsored by NASA.
- **SPECIAL PUBLICATION.** Scientific, technical, or historical information from NASA programs, projects, and missions, often concerned with subjects having substantial public interest.
- **TECHNICAL TRANSLATION.** English-language translations of foreign scientific and technical material pertinent to NASA's mission.

Specialized services that complement the STI Program Office's diverse offerings include creating custom thesauri, building customized data bases, organizing and publishing research results . . . even providing videos.

For more information about the NASA STI Program Office, see the following:

- Access the NASA STI Program Home Page at <http://www.sti.nasa.gov>
- E-mail your question via the Internet to help@sti.nasa.gov
- Fax your question to the NASA Access Help Desk at 301-621-0134
- Telephone the NASA Access Help Desk at 301-621-0390
- Write to:
NASA Access Help Desk
NASA Center for Aerospace Information
7121 Standard Drive
Hanover, MD 21076



High-Fidelity Generalization Method of Cells for Inelastic Periodic Multiphase Materials

Jacob Aboudi
Tel-Aviv University, Ramat-Aviv, Israel

Marek-Jerzy Pindera
University of Virginia, Charlottesville, Virginia

Steven M. Arnold
Glenn Research Center, Cleveland, Ohio

National Aeronautics and
Space Administration

Glenn Research Center

Acknowledgments

This research was conducted under funding through the NASA Glenn Grant NAG3-2524. The authors gratefully acknowledge the contribution of Mr. Daniel Butler of the Civil Engineering Department at the University of Virginia who generated the finite-element results presented in Figures 14, 16, 18, 20, and 23.

Available from

NASA Center for Aerospace Information
7121 Standard Drive
Hanover, MD 21076

National Technical Information Service
5285 Port Royal Road
Springfield, VA 22100

Available electronically at <http://gltrs.grc.nasa.gov/GLTRS>

High-Fidelity Generalized Method of Cells for Inelastic Periodic Multiphase Materials

Jacob Aboudi
Tel-Aviv University
Ramat-Aviv 69978, Israel

Marek-Jerzy Pindera
University of Virginia
Charlottesville, Virginia 22903

Steven M. Arnold
National Aeronautics and Space Administration
Glenn Research Center
Cleveland, Ohio 44135

Abstract

An extension of a recently-developed linear thermoelastic theory for multiphase periodic materials is presented which admits inelastic behavior of the constituent phases. The extended theory is capable of accurately estimating both the effective inelastic response of a periodic multiphase composite and the local stress and strain fields in the individual phases. The model is presently limited to materials characterized by constituent phases that are continuous in one direction, but arbitrarily distributed within the repeating unit cell which characterizes the material's periodic microstructure. The model's analytical framework is based on the homogenization technique for periodic media, but the method of solution for the local displacement and stress fields borrows concepts previously employed by the authors in constructing the higher-order theory for functionally graded materials, in contrast with the standard finite-element solution method typically used in conjunction with the homogenization technique. The present approach produces a closed-form macroscopic constitutive equation for a periodic multiphase material valid for both uniaxial and multiaxial loading. The model's predictive accuracy in generating **both** the effective inelastic stress-strain response and the local stress and inelastic strain fields is demonstrated by comparison with the results of an analytical inelastic solution for the axisymmetric and axial shear response of a unidirectional composite based on the concentric cylinder model, and with finite-element results for transverse loading.

1 Introduction

Micromechanical modeling of multiphase materials with inelastic phases continues to be a challenging problem due to the path-dependence of the local field variables which govern the overall or macroscopic behavior of the material. The relationship between the local and global variables through the use of Hill's strain or stress concentration tensors, Hill (1963), which define the instantaneous macroscopic response, must be established at each instant along the loading path. This is in contrast with the elastic problem which requires determination of Hill's concentration tensors just once.

Many different approaches with varying degrees of complexity and limitations have been proposed for modeling the inelastic response of multiphase materials, cf. Dvorak (2000) for a recent review article. Models for which exact analytical inelastic solutions of the governing field equations are available are limited to the concentric cylinder geometry under axisymmetric or axial shear (but not transverse) loading, Pindera *et al.* (1993) and Williams and Pindera (1997). Finite-element analyses of repeating unit cells representative of materials with periodic microstructures produce very accurate estimates of the local field variables, albeit at a substantial computational cost. The construction of inelastic macroscopic constitutive equations for arbitrary loading based on such analyses is not straightforward, making it difficult to embed finite-element based models into more general structural analysis procedures. This has given rise to the development of approximate models which employ simplifying assumptions on the form of displacement or stress fields within the individual phases. The effect of the inelastic response of the matrix phase is often accounted for through the average values of the inelastic strain field either in the entire matrix phase or in the subvolumes into which the matrix phase is partitioned.

A number of approximate analyses of a repeating unit cell, which employ subvolume discretization of the unit cell to mimic the material's microstructure, has been developed to deal with the inelastic response of periodic multiphase materials. The Generalized Method of Cells, Paley and Aboudi (1992), employs a first-order representation of the displacement field in each subcell of the repeating unit cell, producing **piece-wise uniform** strain and stress fields throughout the cell. The method is a generalization of the original Method of Cells developed by Aboudi (1982) which is based on a limited cell discretization. In the context of unidirectional composites, the generalized version allows accurate and efficient analysis of the impact of fiber shape and arrangement on the composite's inelastic macroscopic response, as demonstrated by Arnold *et al.* (1996). The predictive capability of the method in various applications has been recently summarized by Aboudi (1996). However, despite the method's demonstrated accuracy in modeling the inelastic *macroscopic* response of periodic composites, the accuracy with which local stress and strain fields are captured (although acceptable in many applications) is not as good. This, for instance, requires the incorporation of additional assumptions and modifications into the model's framework in order to trace the evolution of damage at the local level due, for instance, to fiber breakage and fiber/matrix debonding, Bednarczyk and Arnold (2001a,b) and Pahr and Arnold (2001).

The assumption of **piece-wise uniform** strain fields has also been employed by Dvorak (1992) in the context of a procedure called the Transformation Field Analysis. This approach has recently been generalized by Chaboche *et al.* (2001) and demonstrated to capture the local stress and (inelastic) strain fields with good accuracy in comparison to finite-element simulations. Methods which employ more accurate field representations within the repeating unit cell of a periodic composite, albeit at a significantly enhanced computational cost, have been developed by Walker *et al.* (1994) and Fotiu and Nemat-Nasser (1996). These are based on Fourier series approximations of the stress and strain fields within the repeating unit cell. In practice, the solution of the local field quantities is obtained by discretizing the cell into square or triangular subvolumes in which the eigenstrains are assumed to be uniform.

Most recently, a new method for the analysis of the thermoelastic response of multiphase periodic materials, characterized by repeating unit cells with arbitrary microstructures in the plane normal to the direction of the continuous reinforcement (admitting fully anisotropic behavior in this plane), was developed in which the displacement field within each subvolume of the repeating unit cell was approximated by quadratic functions expressed in local coordinates, Aboudi *et al.* (2001). This, in turn, produces **linear** strain and stress fields at the local subvolume level, in contrast with the **piece-wise uniform** fields employed in the Generalized Method of Cells and Transformation Field Analysis. The method's analytical framework is based on the homogenization technique (cf. Sanchez-Palencia, 1980; Suquet, 1987; Parton and Kudryavtsev, 1993; Kalamkarov and Kolpakov, 1997), but the solution procedure for the local displacement, strain and stress fields within each subvolume of the repeating unit cell borrows concepts previously employed by the authors in constructing the higher-order theory for functionally graded materials, Aboudi *et al.* (1999). The

higher-order subvolume displacement representation relative to that employed in the Generalized Method of Cells provides the necessary shear-coupling between the local normal and shear deformation fields and the macroscopically applied average strains. This feature, in turn, produces excellent estimates of **both** the effective thermoelastic moduli of periodic composites and the local stress and strain fields in the individual constituents, as demonstrated in Aboudi *et al.* (2001) through comparison with the finite-element results of Sun and Vaidya (1996) for the effective moduli and an analytical solution for the local stress fields. Therefore, in view of the above features and the same volume discretization methodology as that employed in the Generalized Method of Cells, we refer to this new method as High-Fidelity Generalized Method of Cells or HFGMC.

Herein, an extension of this method is presented which accounts for the inelastic behavior of the individual phases. The method's fully analytical nature results in a closed-form expression for the effective response of a periodic multiphase material under multiaxial loading given in the form of a macroscopic thermoinelastic stress-strain relationship, which can easily be incorporated into a structural analysis code as a subroutine. The ease of the repeating unit cell's construction and the demonstrated accuracy of the theory in predicting the average and the local stress and plastic strain fields, facilitates quick, efficient and reliable analysis of the impact of a multiphase material's microstructure on the average and local response. The theory's accuracy is validated based on comparison with the analytical concentric cylinder model predictions for axisymmetric and axial shear loading, and finite-element predictions for transverse loading. Further, comparison with the predictions of the original Generalized Method of Cells is presented in order to illustrate the advantages derived from the new approach. This comparison also provides an explanation for the good accuracy of the Generalized Method of Cells at the macroscopic level despite poor estimates of certain stress components at the microscopic level.

2 Theoretical Framework

Consider a multiphase composite wherein the microstructure is periodically distributed in the plane $x_2 - x_3$ defined by the global coordinates (x_2, x_3) , see Fig. 1 where the repeating unit cell used to construct the periodic array is highlighted. In the framework of the homogenization method, the displacements are asymptotically expanded as follows

$$u_i(\mathbf{x}, \mathbf{y}) = u_{0i}(\mathbf{x}, \mathbf{y}) + \delta u_{1i}(\mathbf{x}, \mathbf{y}) + \delta^2 u_{2i}(\mathbf{x}, \mathbf{y}) + \dots \quad (1)$$

where $\mathbf{x} = (x_1, x_2, x_3)$ are the macroscopic (global) coordinates, and $\mathbf{y} = (y_1, y_2, y_3)$ are the microscopic (local) coordinates that are defined with respect to the repeating unit cell. The material's periodicity imposes the constraint $u_{\alpha i}(\mathbf{x}, \mathbf{y}) = u_{\alpha i}(\mathbf{x}, \mathbf{y} + n_p \mathbf{d}_p)$ on the different-order terms $u_{\alpha i}$ ($\alpha = 0, 1, 2, \dots$) in Eq. (1), where n_p are arbitrary integer numbers and the constant vectors \mathbf{d}_p characterize the material's periodicity. In addition, the size of the unit cell is further assumed to be much smaller than the size of the body so that the relation between the global and local systems is $y_i = x_i/\delta$, where δ is a small scaling parameter characterizing the size of the unit cell. This implies that a movement of order unity on the local scale corresponds to a very small movement on the global scale.

Employing the following relation in evaluating the derivative of a field quantity:

$$\frac{\partial}{\partial x_i} \rightarrow \frac{\partial}{\partial x_i} + \frac{1}{\delta} \frac{\partial}{\partial y_i} \quad (2)$$

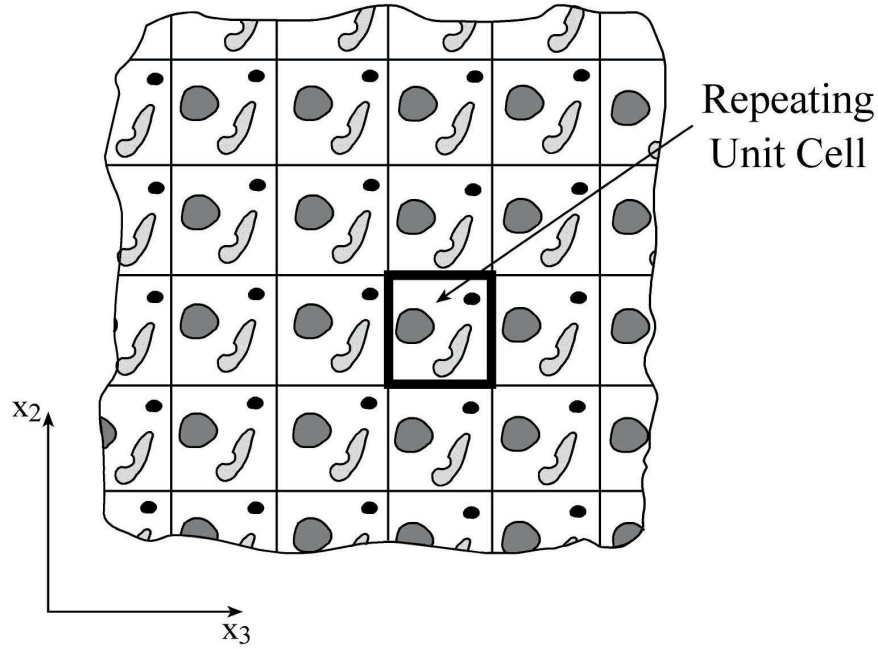


Figure 1. A multi-phase composite with a periodic microstructure in the $x_2 - x_3$ plane characterized by a repeating unit cell (highlighted).

the strain components are determined from the displacement expansion (1) in the following form

$$\epsilon_{ij} = \bar{\epsilon}_{ij}(\mathbf{x}) + \tilde{\epsilon}_{ij}(\mathbf{x}, \mathbf{y}) + O(\delta) \quad (3)$$

where the average and fluctuating strains, $\bar{\epsilon}_{ij}(\mathbf{x})$ and $\tilde{\epsilon}_{ij}(\mathbf{x}, \mathbf{y})$, are given by global and local strain-displacement relations as follows

$$\bar{\epsilon}_{ij}(\mathbf{x}) = \frac{1}{2} \left(\frac{\partial \bar{u}_i}{\partial x_j} + \frac{\partial \bar{u}_j}{\partial x_i} \right), \quad \tilde{\epsilon}_{ij}(\mathbf{x}, \mathbf{y}) = \frac{1}{2} \left(\frac{\partial \tilde{u}_i}{\partial y_j} + \frac{\partial \tilde{u}_j}{\partial y_i} \right) \quad (4)$$

In the above equation, \bar{u}_i are displacement components in the homogenized region (at the continuum scale) and hence are not functions of the local coordinates \mathbf{y} , and $u_{1i} = \tilde{u}_i$ are the fluctuating displacements. It can be easily shown that

$$\frac{1}{V_y} \int \epsilon_{ij} dV_y = \frac{1}{V_y} \int (\bar{\epsilon}_{ij} + \tilde{\epsilon}_{ij}) dV_y = \bar{\epsilon}_{ij}$$

where V_y is the volume of the repeating unit cell. This follows directly from the periodicity of the fluctuating strain, implying that the average of the fluctuating strain taken over the unit repeating cell vanishes.

Using Eq. (3), one can readily represent the displacements in the form

$$u_i(\mathbf{x}, \mathbf{y}) = \bar{\epsilon}_{ij} x_j + \tilde{u}_i + O(\delta^2) \quad (5)$$

where $\bar{\epsilon}_{ij} x_j$ represents the contribution of the average (homogenized) strain to the total displacement field and \tilde{u}_i represents the fluctuating displacement field. This representation will be employed in constructing an approximate displacement field for the solution of the cell problem discussed in Section 2.2.

For given values of the average strains $\bar{\epsilon}_{ij}$, the unknown fluctuating displacements are governed by the equilibrium equations subject to periodic boundary conditions imposed on the displacement and traction

components that are prescribed at the boundaries of the repeating unit cell. In addition to these boundary conditions one needs to impose the continuity of displacements and tractions at the internal interfaces between the phases that fill the repeating unit cell. The manner of solving the governing field equations for the fluctuating displacements in the repeating unit cell based on the representation given by Eq. (5) is described next.

2.1 Definition of the cell problem

We perform the analysis on the repeating unit cell which occupies the region $0 \leq y_2 \leq H$, $0 \leq y_3 \leq L$ specified in terms of the local coordinates (y_2, y_3) . The microstructure of the repeating unit cell in the $y_2 - y_3$ plane in the given region is discretized into N_q and N_r internal or generic cells. Figure 2(a) illustrates how the repeating unit cell highlighted in Fig. 1 could be discretized. In addition, every generic cell consists of four subcells designated by the pair $(\beta\gamma)$ where each index takes the value 1 or 2 which indicates the relative position of the given subcell along the y_2 and y_3 axis, respectively, see Fig. 2(b). The indices q and r , whose ranges are $q = 1, 2, \dots, N_q$ and $r = 1, 2, \dots, N_r$, identify the generic cell in the $y_2 - y_3$ plane. The dimensions of the generic cell along the y_2 and y_3 axes are $h_1^{(q)}, h_2^{(q)}$ and $l_1^{(r)}, l_2^{(r)}$, such that $H = \sum_{q=1}^{N_q} (h_1^{(q)} + h_2^{(q)})$, $L = \sum_{r=1}^{N_r} (l_1^{(r)} + l_2^{(r)})$. This manner of discretizing a periodic material's microstructure has also been employed in constructing the original Generalized Method of Cells (Paley and Aboudi, 1992). The construction of the higher-order theory for functionally graded materials, characterized by spatially variable microstructures without a definable repeating unit cell, is also based on such volume discretization (Aboudi *et al.* 1999).

Given an applied macroscopic loading specified by the average strains $\bar{\epsilon}_{ij}$, an approximate solution for the displacement field within each $(\beta\gamma)$ subcell of the $N_q N_r$ generic cells is constructed based on volumetric averaging of the equilibrium equations together with the imposition of periodic boundary conditions, and both the displacement and traction continuity conditions, in an average sense between the cells and subcells used to characterize the material's microstructure. The equilibrium equations for the $(\beta\gamma)$ subcell occupying the region $|\bar{y}_2^{(\beta)}| \leq h_\beta^{(q)}/2$, $|\bar{y}_3^{(\gamma)}| \leq l_\gamma^{(r)}/2$ that the displacement field must satisfy are given by

$$\partial_2 \sigma_{2j}^{(\beta\gamma)} + \partial_3 \sigma_{3j}^{(\beta\gamma)} = 0 \quad j = 1, 2, 3 \quad (6)$$

where $\partial_2 = \partial/\partial \bar{y}_2^{(\beta)}$ and $\partial_3 = \partial/\partial \bar{y}_3^{(\gamma)}$. The subcell stress components are related to the subcell strains through generalized Hooke's Law which includes spatially uniform thermal loading characterized by the temperature deviation ΔT from a reference temperature and inelastic effects,

$$\sigma_{ij}^{(\beta\gamma)} = C_{ijkl}^{(\beta\gamma)} (\epsilon_{kl}^{(\beta\gamma)} - \epsilon_{kl}^{I(\beta\gamma)} - \epsilon_{kl}^{T(\beta\gamma)}) \quad (7)$$

where $C_{ijkl}^{(\beta\gamma)}$ are the elements of the stiffness tensor of the $(\beta\gamma)$ subcell, $\epsilon_{kl}^{(\beta\gamma)}$ are the total strains, and $\epsilon_{kl}^{I(\beta\gamma)}$, $\epsilon_{kl}^{T(\beta\gamma)}$ are the inelastic and thermal strains in the subcell, with no summation implied by repeated Greek letters in the above and henceforth. The inelastic strains are derived from the chosen inelastic constitutive model. In this paper, we consider either elastic orthotropic materials (characterized by nine independent $C_{ijkl}^{(\beta\gamma)}$ elements) or inelastic materials which are isotropic in both elastic and inelastic domains. Hence, Eq. (7) reduces to (assuming incompressibility of the inelastic strains)

$$\sigma_{ij}^{(\beta\gamma)} = C_{ijkl}^{(\beta\gamma)} \epsilon_{kl}^{(\beta\gamma)} - 2\mu^{(\beta\gamma)} \epsilon_{ij}^{I(\beta\gamma)} - \sigma_{ij}^{T(\beta\gamma)} \quad (8)$$

where $\mu^{(\beta\gamma)}$ is the elastic shear modulus of the material filling the given subcell $(\beta\gamma)$, and the term $\sigma_{ij}^{T(\beta\gamma)}$, henceforth referred to as thermal stress, stands for the thermal contribution

$$\sigma_{ij}^{T(\beta\gamma)} = \Gamma_{ij}^{(\beta\gamma)} \Delta T \quad (9)$$

where $\Gamma_{ij}^{(\beta\gamma)}$ are the thermal stress coefficients. We relate the subcell displacement field, which forms the basis for the solution of the equilibrium equations, to the subcell stresses through the Hooke's Law (7) in conjunction with the subcell strain-displacement equations. Taking into account Eqs. (3) and (4), the total strains in the subcell $(\beta\gamma)$ are given by

$$\epsilon_{ij}^{(\beta\gamma)} = \bar{\epsilon}_{ij} + \frac{1}{2}(\partial_i u_j^{(\beta\gamma)} + \partial_j u_i^{(\beta\gamma)}) \quad (10)$$

where $\partial_1 = 0$ and ∂_2, ∂_3 have been defined previously.

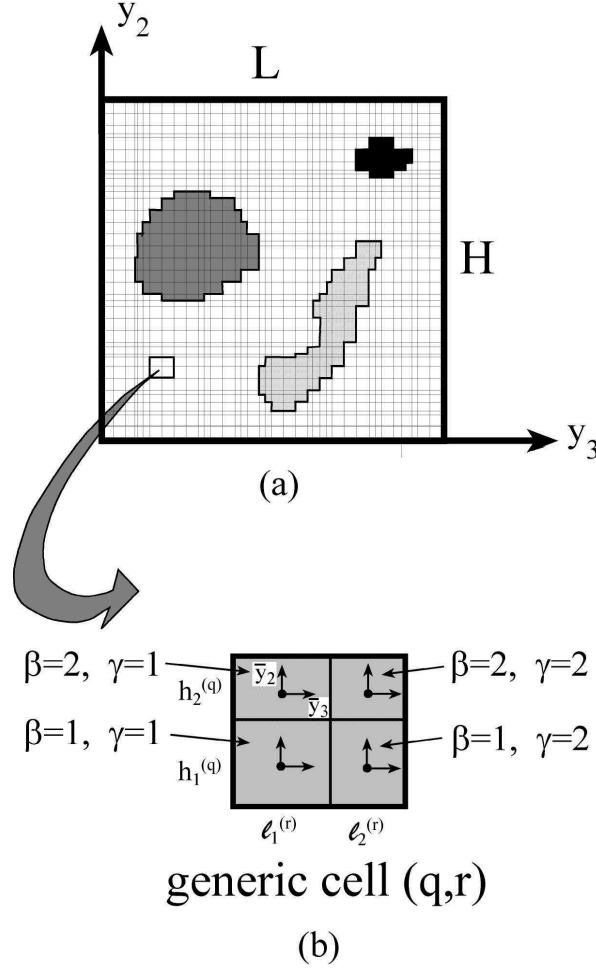


Figure 2. (a) Volume discretization of the repeating unit cell employed in the present model, (b) generic cell within the repeating unit cell.

2.2 Method of solution for the cell problem

We begin the solution of the equilibrium equations by approximating the fluctuating displacements in each subcell using a quadratic expansion in terms of local coordinates $(\bar{y}_2^{(\beta)}, \bar{y}_3^{(\gamma)})$ centered at the subcell's midpoint. This is in sharp contrast with the original Generalized Method of Cells where the employed displacement expansion was linear as a result of which the coupling between the local normal and shear effects was

lost. A higher-order representation of the fluctuating displacement field is necessary in order to capture the local effects created by the field gradients and the microstructure of the composite. This was demonstrated within the framework of the elastic version of the High-Fidelity Generalized Method of Cells in the context of the problem of an infinite plate with a circular inclusion subjected to a far-field uniform stress (Aboudi *et al.* 2001). Both qualitative and quantitative aspects of the local stress field within the inclusion and its vicinity, as well as the asymptotic character of the stress field away from the inclusion, were captured with very good accuracy upon comparison with the exact analytical solution. Such local effects cannot be captured by the original Generalized Method of Cells due the first-order (linear) displacement representation within each subcell (which produces piece-wise uniform strain and stress fields within the repeating unit cell), and the imposition of traction continuity conditions at the subcell interfaces in an average sense. As a consequence, tractions along each column of subcells spanning the representative volume element in the directions associated with the particular traction components are uniform, precluding the possibility of modeling local effects due to matrix-inclusion as well as adjacent inclusion interactions (Pindera and Bednarczyk, 1999). This shortcoming has been eliminated by the present theory as previously demonstrated in the elastic case and as will be demonstrated in the inelastic case considered in the current contribution.

Following the general displacement representation for periodic media given by Eq. (5), the subcell displacement approximation in the High-Fidelity Generalized Method of Cells has the form (omitting the cell label (q, r) , see Fig. 2b),

$$\begin{aligned} u_1^{(\beta\gamma)} &= \bar{\epsilon}_{1j}x_j + W_{1(00)}^{(\beta\gamma)} + \bar{y}_2^{(\beta)}W_{1(10)}^{(\beta\gamma)} + \bar{y}_3^{(\gamma)}W_{1(01)}^{(\beta\gamma)} \\ &+ \frac{1}{2}(3\bar{y}_2^{(\beta)2} - \frac{h_\beta^{(q)2}}{4})W_{1(20)}^{(\beta\gamma)} + \frac{1}{2}(3\bar{y}_3^{(\gamma)2} - \frac{l_\gamma^{(r)2}}{4})W_{1(02)}^{(\beta\gamma)} \end{aligned} \quad (11)$$

$$\begin{aligned} u_2^{(\beta\gamma)} &= \bar{\epsilon}_{2j}x_j + W_{2(00)}^{(\beta\gamma)} + \bar{y}_2^{(\beta)}W_{2(10)}^{(\beta\gamma)} + \bar{y}_3^{(\gamma)}W_{2(01)}^{(\beta\gamma)} \\ &+ \frac{1}{2}(3\bar{y}_2^{(\beta)2} - \frac{h_\beta^{(q)2}}{4})W_{2(20)}^{(\beta\gamma)} + \frac{1}{2}(3\bar{y}_3^{(\gamma)2} - \frac{l_\gamma^{(r)2}}{4})W_{2(02)}^{(\beta\gamma)} \end{aligned} \quad (12)$$

$$\begin{aligned} u_3^{(\beta\gamma)} &= \bar{\epsilon}_{3j}x_j + W_{3(00)}^{(\beta\gamma)} + \bar{y}_2^{(\beta)}W_{3(10)}^{(\beta\gamma)} + \bar{y}_3^{(\gamma)}W_{3(01)}^{(\beta\gamma)} \\ &+ \frac{1}{2}(3\bar{y}_2^{(\beta)2} - \frac{h_\beta^{(q)2}}{4})W_{3(20)}^{(\beta\gamma)} + \frac{1}{2}(3\bar{y}_3^{(\gamma)2} - \frac{l_\gamma^{(r)2}}{4})W_{3(02)}^{(\beta\gamma)} \end{aligned} \quad (13)$$

where $W_{i(00)}^{(\beta\gamma)}$ are the fluctuating volume-averaged displacements, and $W_{i(mn)}^{(\beta\gamma)}$ ($i = 1, 2, 3$) are the higher-order terms. The number of these unknown microvariables that describe the fluctuating displacements in the cell (q, r) is 60. These microvariables are determined by satisfying the equilibrium equations (6) in a volumetric sense, the interfacial continuity conditions (both displacements and tractions) on the faces separating adjacent subcells and cells in an integral sense,

$$\begin{aligned} \int_{-l_\gamma/2}^{l_\gamma/2} \sigma_{2j}^{(1\gamma)} \Big|_{\bar{y}_2^{(1)}=h_1/2}^{(q,r)} d\bar{y}_3^{(\gamma)} &= \int_{-l_\gamma/2}^{l_\gamma/2} \sigma_{2j}^{(2\gamma)} \Big|_{\bar{y}_2^{(2)}=-h_2/2}^{(q,r)} d\bar{y}_3^{(\gamma)} \\ \int_{-h_\beta/2}^{h_\beta/2} \sigma_{3j}^{(\beta 1)} \Big|_{\bar{y}_3^{(1)}=l_1/2}^{(q,r)} d\bar{y}_2^{(\beta)} &= \int_{-h_\beta/2}^{h_\beta/2} \sigma_{3j}^{(\beta 2)} \Big|_{\bar{y}_3^{(2)}=-l_2/2}^{(q,r)} d\bar{y}_2^{(\beta)} \end{aligned}$$

$$\begin{aligned}
\int_{-l_\gamma/2}^{l_\gamma/2} \sigma_{2j}^{(1\gamma)} \Big|_{\frac{y_2^{(1)}}{y_2} = -h_1/2}^{(q+1,r)} d\bar{y}_3^{(\gamma)} &= \int_{-l_\gamma/2}^{l_\gamma/2} \sigma_{2j}^{(2\gamma)} \Big|_{\frac{y_2^{(2)}}{y_2} = h_2/2}^{(q,r)} d\bar{y}_3^{(\gamma)} \\
\int_{-h_\beta/2}^{h_\beta/2} \sigma_{3j}^{(\beta 1)} \Big|_{\frac{y_3^{(1)}}{y_3} = -l_1/2}^{(q,r+1)} d\bar{y}_2^{(\beta)} &= \int_{-h_\beta/2}^{h_\beta/2} \sigma_{3j}^{(\beta 2)} \Big|_{\frac{y_3^{(2)}}{y_3} = l_2/2}^{(q,r)} d\bar{y}_2^{(\beta)} \\
\int_{-l_\gamma/2}^{l_\gamma/2} \tilde{u}_i^{(1\gamma)} \Big|_{\frac{y_2^{(1)}}{y_2} = h_1/2}^{(q,r)} d\bar{y}_3^{(\gamma)} &= \int_{-l_\gamma/2}^{l_\gamma/2} \tilde{u}_i^{(2\gamma)} \Big|_{\frac{y_2^{(2)}}{y_2} = -h_2/2}^{(q,r)} d\bar{y}_3^{(\gamma)} \\
\int_{-h_\beta/2}^{h_\beta/2} \tilde{u}_i^{(\beta 1)} \Big|_{\frac{y_3^{(1)}}{y_3} = l_1/2}^{(q,r)} d\bar{y}_2^{(\beta)} &= \int_{-h_\beta/2}^{h_\beta/2} \tilde{u}_i^{(\beta 2)} \Big|_{\frac{y_3^{(2)}}{y_3} = -l_2/2}^{(q,r)} d\bar{y}_2^{(\beta)} \\
\int_{-l_\gamma/2}^{l_\gamma/2} \tilde{u}_i^{(1\gamma)} \Big|_{\frac{y_2^{(1)}}{y_2} = -h_1/2}^{(q+1,r)} d\bar{y}_3^{(\gamma)} &= \int_{-l_\gamma/2}^{l_\gamma/2} \tilde{u}_i^{(2\gamma)} \Big|_{\frac{y_2^{(2)}}{y_2} = h_2/2}^{(q,r)} d\bar{y}_3^{(\gamma)} \\
\int_{-h_\beta/2}^{h_\beta/2} \tilde{u}_i^{(\beta 1)} \Big|_{\frac{y_3^{(1)}}{y_3} = -l_1/2}^{(q,r+1)} d\bar{y}_2^{(\beta)} &= \int_{-h_\beta/2}^{h_\beta/2} \tilde{u}_i^{(\beta 2)} \Big|_{\frac{y_3^{(2)}}{y_3} = l_2/2}^{(q,r)} d\bar{y}_2^{(\beta)}
\end{aligned} \tag{14}$$

and the periodic boundary conditions at $y_2 = 0, H$ and $y_3 = 0, L$ expressed in the local subcell coordinates for the appropriate subcells within the boundary generic cells

$$\begin{aligned}
\int_{-l_\gamma/2}^{l_\gamma/2} \sigma_{2j}^{(1\gamma)} \Big|_{\frac{y_2^{(1)}}{y_2} = -h_1/2}^{(1,r)} d\bar{y}_3^{(\gamma)} &= \int_{-l_\gamma/2}^{l_\gamma/2} \sigma_{2j}^{(2\gamma)} \Big|_{\frac{y_2^{(2)}}{y_2} = h_2/2}^{(N_q,r)} d\bar{y}_3^{(\gamma)} \\
\int_{-h_\beta/2}^{h_\beta/2} \sigma_{3j}^{(\beta 1)} \Big|_{\frac{y_3^{(1)}}{y_3} = -l_1/2}^{(q,1)} d\bar{y}_2^{(\beta)} &= \int_{-h_\beta/2}^{h_\beta/2} \sigma_{3j}^{(\beta 2)} \Big|_{\frac{y_3^{(2)}}{y_3} = l_2/2}^{(q,N_r)} d\bar{y}_2^{(\beta)} \\
\int_{-l_\gamma/2}^{l_\gamma/2} \tilde{u}_i^{(1\gamma)} \Big|_{\frac{y_2^{(1)}}{y_2} = -h_1/2}^{(1,r)} d\bar{y}_3^{(\gamma)} &= \int_{-l_\gamma/2}^{l_\gamma/2} \tilde{u}_i^{(2\gamma)} \Big|_{\frac{y_2^{(2)}}{y_2} = h_2/2}^{(N_q,r)} d\bar{y}_3^{(\gamma)} \\
\int_{-h_\beta/2}^{h_\beta/2} \tilde{u}_i^{(\beta 1)} \Big|_{\frac{y_3^{(1)}}{y_3} = -l_1/2}^{(q,1)} d\bar{y}_2^{(\beta)} &= \int_{-h_\beta/2}^{h_\beta/2} \tilde{u}_i^{(\beta 2)} \Big|_{\frac{y_3^{(2)}}{y_3} = l_2/2}^{(q,N_r)} d\bar{y}_2^{(\beta)}
\end{aligned} \tag{15}$$

where $i, j = 1, 2, 3$. These periodicity conditions ensure that the repeating unit cell is an integral part of the periodic array representing the entire multiphase material, thereby explicitly accounting for the interaction with the adjacent unit cells. As shown in the following development, application of these conditions produces the correct number of equations for the determination of the unknown microvariables.

In the perfectly elastic case, the above displacement expansions produce linear variations in strains and stresses at each point within the subcell. In the presence of inelastic effects, however, a linear strain generated by these equations does not imply the linearity of the stress field due to the path-dependent deformation. Thus the displacement field microvariables must depend implicitly on the inelastic strain distributions, giving rise to a higher-order stress field than the linear strain field generated from the assumed displacement field representation. In the presence of inelastic effects, this higher-order stress field is represented by a higher-order Legendre polynomial expansion in the local coordinates. Therefore, the strain field generated from the assumed displacement field, and the resulting stress field, must also be expressed in terms of Legendre polynomials:

$$\epsilon_{ij}^{(\beta\gamma)} = \sum_{m=0}^{\infty} \sum_{n=0}^{\infty} \sqrt{(1+2m)(1+2n)} e_{ij(m,n)}^{(\beta\gamma)} P_m(\zeta_2^{(\beta)}) P_n(\zeta_3^{(\gamma)}) \quad (16)$$

$$\sigma_{ij}^{(\beta\gamma)} = \sum_{m=0}^{\infty} \sum_{n=0}^{\infty} \sqrt{(1+2m)(1+2n)} \tau_{ij(m,n)}^{(\beta\gamma)} P_m(\zeta_2^{(\beta)}) P_n(\zeta_3^{(\gamma)}) \quad (17)$$

where the non-dimensional variables $\zeta_i^{(\cdot)}$, defined in the interval $-1 \leq \zeta_i^{(\cdot)} \leq 1$, are given in terms of the local subcell coordinates as $\zeta_2^{(\beta)} = \bar{y}_2^{(\beta)} / (h_\beta^{(q)} / 2)$, and $\zeta_3^{(\gamma)} = \bar{y}_3^{(\gamma)} / (l_\gamma^{(r)} / 2)$. For the given displacement field representation, the upper limits on the summations in Eq. (16) become 1. The upper limits on the summations in Eq. (17) are chosen so that an accurate representation of the stress field (which depends on the amount of the inelastic flow) is obtained within each subcell, Aboudi *et al.* (1999). The coefficients $e_{ij(m,n)}^{(\beta\gamma)}, \tau_{ij(m,n)}^{(\beta\gamma)}$ in the above expansions are determined as described below.

The strain coefficients $e_{ij(m,n)}^{(\beta\gamma)}$ in subcell $(\beta\gamma)$ of cell (q, r) are explicitly determined in terms of the displacement field using the orthogonal properties of Legendre polynomials. The non-zero components are given as follows (omitting (q, r))

$$\begin{aligned} e_{11(0,0)}^{(\beta\gamma)} &= \bar{\epsilon}_{11} \\ e_{22(0,0)}^{(\beta\gamma)} &= \bar{\epsilon}_{22} + W_{2(10)}^{(\beta\gamma)} \\ e_{22(1,0)}^{(\beta\gamma)} &= \frac{\sqrt{3}}{2} h_\beta^{(q)} W_{2(20)}^{(\beta\gamma)} \\ e_{33(0,0)}^{(\beta\gamma)} &= \bar{\epsilon}_{33} + W_{3(01)}^{(\beta\gamma)} \\ e_{33(0,1)}^{(\beta\gamma)} &= \frac{\sqrt{3}}{2} l_\gamma^{(r)} W_{3(02)}^{(\beta\gamma)} \\ e_{23(0,0)}^{(\beta\gamma)} &= \bar{\epsilon}_{23} + \frac{1}{2} (W_{2(01)}^{(\beta\gamma)} + W_{3(10)}^{(\beta\gamma)}) \\ e_{23(1,0)}^{(\beta\gamma)} &= \frac{\sqrt{3}}{4} h_\beta^{(q)} W_{3(20)}^{(\beta\gamma)} \\ e_{23(0,1)}^{(\beta\gamma)} &= \frac{\sqrt{3}}{4} l_\gamma^{(r)} W_{2(02)}^{(\beta\gamma)} \\ e_{13(0,0)}^{(\beta\gamma)} &= \bar{\epsilon}_{13} + \frac{1}{2} W_{1(01)}^{(\beta\gamma)} \\ e_{13(0,1)}^{(\beta\gamma)} &= \frac{\sqrt{3}}{4} l_\gamma^{(r)} W_{1(02)}^{(\beta\gamma)} \end{aligned}$$

$$\begin{aligned}
e_{12(0,0)}^{(\beta\gamma)} &= \bar{\epsilon}_{12} + \frac{1}{2}W_{1(10)}^{(\beta\gamma)} \\
e_{12(1,0)}^{(\beta\gamma)} &= \frac{\sqrt{3}}{4}h_{\beta}^{(q)}W_{1(20)}^{(\beta\gamma)}
\end{aligned} \tag{18}$$

It should be noted that $e_{ij(0,0)}^{(\beta\gamma)}$ provide the average strains in subcell $(\beta\gamma)$ of cell (q, r) .

The stress coefficients $\tau_{ij(m,n)}^{(\beta\gamma)}$ in subcell $(\beta\gamma)$ of cell (q, r) are expressed in terms of the strain coefficients, thermal stress and the unknown inelastic strain distributions, by first substituting the Legendre polynomial representations for the total strain and stress into the constitutive equations, Eq. (8), and then utilizing the orthogonality of Legendre polynomials:

$$\tau_{ij(m,n)}^{(\beta\gamma)} = C_{ijkl}^{(\beta\gamma)} e_{kl(m,n)}^{(\beta\gamma)} - R_{ij(m,n)}^{(\beta\gamma)} - \sigma_{ij}^{T(\beta\gamma)} \delta_{m0} \delta_{n0} \tag{19}$$

The $R_{ij(m,n)}^{(\beta\gamma)}$ terms represent the inelastic stress distributions calculated in the following manner

$$R_{ij(m,n)}^{(\beta\gamma)} = \frac{1}{2}\mu^{(\beta\gamma)} \sqrt{(2m+1)(2n+1)} \int_{-1}^1 \int_{-1}^1 \epsilon_{ij}^{I(\beta\gamma)} P_m(\zeta_2^{(\beta)}) P_n(\zeta_3^{(\gamma)}) d\zeta_2^{(\beta)} d\zeta_3^{(\gamma)} \tag{20}$$

Note that in both Eqs. (19) and (20) the cell labeling (q, r) has been omitted.

In the course of satisfying the equilibrium equations in a volumetric sense, it is convenient to define the following stress quantities:

$$[S_{ij(m,n)}^{(\beta\gamma)}]^{(q,r)} = \frac{1}{h_{\beta}^{(q)} l_{\gamma}^{(r)}} \int_{-h_{\beta}^{(q)}/2}^{h_{\beta}^{(q)}/2} \int_{-l_{\gamma}^{(r)}/2}^{l_{\gamma}^{(r)}/2} \sigma_{ij}^{(\beta\gamma)} (\bar{y}_2^{(\beta)})^m (\bar{y}_3^{(\gamma)})^n d\bar{y}_2^{(\beta)} d\bar{y}_3^{(\gamma)} \tag{21}$$

For $m = n = 0$, Eq. (21) provides the average stresses in the subcell, whereas for other values of (m, n) higher-order stresses are obtained that are needed to describe the governing field equations of the continuum. These stress quantities can be evaluated explicitly in terms of the unknown coefficients $W_{i(mn)}^{(\beta\gamma)}$ by performing the required volume integration upon substituting Eqs. (8), (10) and (11)–(13) in Eq. (21). This yields the following non-vanishing zeroth-order and first-order stress components in terms of the unknown coefficients in the displacement field expansion (omitting (q, r)):

$$S_{11(0,0)}^{(\beta\gamma)} = C_{11}^{(\beta\gamma)} \bar{\epsilon}_{11} + C_{12}^{(\beta\gamma)} (W_{2(10)}^{(\beta\gamma)} + \bar{\epsilon}_{22}) + C_{13}^{(\beta\gamma)} (W_{3(01)}^{(\beta\gamma)} + \bar{\epsilon}_{33}) - \Gamma_1^{(\beta\gamma)} \Delta T - R_{11(0,0)}^{(\beta\gamma)} \tag{22}$$

$$S_{11(1,0)}^{(\beta\gamma)} = \frac{1}{4}h_{\beta}^{(q)2} C_{12}^{(\beta\gamma)} W_{2(20)}^{(\beta\gamma)} - \frac{1}{2\sqrt{3}}h_{\beta}^{(q)} R_{11(1,0)}^{(\beta\gamma)} \tag{23}$$

$$S_{11(0,1)}^{(\beta\gamma)} = \frac{1}{4}l_{\gamma}^{(r)2} C_{13}^{(\beta\gamma)} W_{3(02)}^{(\beta\gamma)} - \frac{1}{2\sqrt{3}}l_{\gamma}^{(r)} R_{11(0,1)}^{(\beta\gamma)} \tag{24}$$

with similar expressions for the other normal stress components, and

$$S_{23(0,0)}^{(\beta\gamma)} = C_{44}^{(\beta\gamma)} (2\bar{\epsilon}_{23} + W_{2(01)}^{(\beta\gamma)} + W_{3(10)}^{(\beta\gamma)}) - R_{23(0,0)}^{(\beta\gamma)} \tag{25}$$

$$S_{23(1,0)}^{(\beta\gamma)} = \frac{1}{4}h_{\beta}^{(q)2} C_{44}^{(\beta\gamma)} W_{3(20)}^{(\beta\gamma)} - \frac{1}{2\sqrt{3}}h_{\beta}^{(q)} R_{23(1,0)}^{(\beta\gamma)} \tag{26}$$

$$S_{23(0,1)}^{(\beta\gamma)} = \frac{1}{4}l_{\gamma}^{(r)2} C_{44}^{(\beta\gamma)} W_{2(02)}^{(\beta\gamma)} - \frac{1}{2\sqrt{3}}l_{\gamma}^{(r)} R_{23(0,1)}^{(\beta\gamma)} \tag{27}$$

$$S_{13(0,0)}^{(\beta\gamma)} = C_{55}^{(\beta\gamma)} (2\bar{\epsilon}_{13} + W_{1(01)}^{(\beta\gamma)}) - R_{13(0,0)}^{(\beta\gamma)} \tag{28}$$

$$S_{13(0,1)}^{(\beta\gamma)} = \frac{1}{4}l_\gamma^{(r)2}C_{55}^{(\beta\gamma)}W_{1(02)}^{(\beta\gamma)} - \frac{1}{2\sqrt{3}}l_\gamma^{(r)}R_{13(0,1)}^{(\beta\gamma)} \quad (29)$$

$$S_{12(0,0)}^{(\beta\gamma)} = C_{66}^{(\beta\gamma)}(2\bar{\epsilon}_{12} + W_{1(10)}^{(\beta\gamma)}) - R_{12(0,0)}^{(\beta\gamma)} \quad (30)$$

$$S_{12(1,0)}^{(\beta\gamma)} = \frac{1}{4}h_\beta^{(q)2}C_{66}^{(\beta\gamma)}W_{1(20)}^{(\beta\gamma)} - \frac{1}{2\sqrt{3}}h_\beta^{(q)}R_{12(1,0)}^{(\beta\gamma)} \quad (31)$$

where contracted notation has been employed for the stiffness elements $C_{ijkl}^{(\beta\gamma)}$.

Subsequently, satisfaction of the zeroth, first, and second moments of the equilibrium equations (6) results in the following 12 relations among the the volume-averaged first-order stresses $S_{ij(m,n)}^{(\beta\gamma)}$ in the different subcells $(\beta\gamma)$ of the (q, r) cell, after lengthy algebraic manipulations

$$[S_{2j(1,0)}^{(\beta\gamma)}/h_\beta^2 + S_{3j(0,1)}^{(\beta\gamma)}/l_\gamma^2]^{(q,r)} = 0 \quad j = 1, 2, 3 \quad (32)$$

The continuity of tractions at the subcell interfaces within each interior cell, and between adjacent cells, imposed in an average sense, can be shown to reduce to the following relations which are obtained from the first four equations of (14) after some algebraic manipulations,

$$[-12S_{2j(1,0)}^{(1\gamma)}/h_1 + S_{2j(0,0)}^{(2\gamma)} - 6S_{2j(1,0)}^{(2\gamma)}/h_2]^{(q,r)} - [S_{2j(0,0)}^{(2\gamma)} + 6S_{2j(1,0)}^{(2\gamma)}/h_2]^{(q-1,r)} = 0 \quad (33)$$

$$[-S_{2j(0,0)}^{(1\gamma)} + \frac{1}{2}S_{2j(0,0)}^{(2\gamma)} - 3S_{2j(1,0)}^{(2\gamma)}/h_2]^{(q,r)} + \frac{1}{2}[S_{2j(0,0)}^{(2\gamma)} + 6S_{2j(1,0)}^{(2\gamma)}/h_2]^{(q-1,r)} = 0 \quad (34)$$

$$[-12S_{3j(0,1)}^{(\beta 1)}/l_1 + S_{3j(0,0)}^{(\beta 2)} - 6S_{3j(0,1)}^{(\beta 2)}/l_2]^{(q,r)} - [S_{3j(0,0)}^{(\beta 2)} + 6S_{3j(0,1)}^{(\beta 2)}/l_2]^{(q,r-1)} = 0 \quad (35)$$

$$[-S_{3j(0,0)}^{(\beta 1)} + \frac{1}{2}S_{3j(0,0)}^{(\beta 2)} - 3S_{3j(0,1)}^{(\beta 2)}/l_2]^{(q,r)} + \frac{1}{2}[S_{3j(0,0)}^{(\beta 2)} + 6S_{3j(0,1)}^{(\beta 2)}/l_2]^{(q,r-1)} = 0 \quad (36)$$

where $j = 1, 2$, and 3 . The details of derivation of equations similar to Eqs. (32)-(36) have been provided by Aboudi *et al.* (1996) for a more general case of a microstructure containing periodic inclusions in the out-of-plane direction.

Equations (33)-(36) provide 24 additional relations among the zeroth-order and first-order stresses. These relations together with Eq. (32), can be expressed in terms of the unknown coefficients $W_{i(mn)}^{(\beta\gamma)}$ by making use of Eqs. (22)-(31), providing a total of 36 of the required 60 equations necessary for the determination of these coefficients in the cell (q, r) .

The additional 24 relations necessary to determine the unknown coefficients in the displacement field expansion are subsequently obtained by imposing displacement continuity conditions on an average basis at each subcell and cell interface. This produces, upon use of the last four equations of (14),

$$[W_{i(00)}^{(1\gamma)} + \frac{1}{2}h_1W_{i(10)}^{(1\gamma)} + \frac{1}{4}h_1^2W_{i(20)}^{(1\gamma)}]^{(q,r)} = [W_{i(00)}^{(2\gamma)} - \frac{1}{2}h_2W_{i(10)}^{(2\gamma)} + \frac{1}{4}h_2^2W_{i(20)}^{(2\gamma)}]^{(q,r)} \quad (37)$$

$$[W_{i(00)}^{(2\gamma)} + \frac{1}{2}h_2W_{i(10)}^{(2\gamma)} + \frac{1}{4}h_2^2W_{i(20)}^{(2\gamma)}]^{(q,r)} = [W_{i(00)}^{(1\gamma)} - \frac{1}{2}h_1W_{i(10)}^{(1\gamma)} + \frac{1}{4}h_1^2W_{i(20)}^{(1\gamma)}]^{(q+1,r)} \quad (38)$$

$$[W_{i(00)}^{(\beta 1)} + \frac{1}{2}l_1W_{i(01)}^{(\beta 1)} + \frac{1}{4}l_1^2W_{i(02)}^{(\beta 1)}]^{(q,r)} = [W_{i(00)}^{(\beta 2)} - \frac{1}{2}l_2W_{i(01)}^{(\beta 2)} + \frac{1}{4}l_2^2W_{i(02)}^{(\beta 2)}]^{(q,r)} \quad (39)$$

$$[W_{i(00)}^{(\beta 2)} + \frac{1}{2}l_2W_{i(01)}^{(\beta 2)} + \frac{1}{4}l_2^2W_{i(02)}^{(\beta 2)}]^{(q,r)} = [W_{i(00)}^{(\beta 1)} - \frac{1}{2}l_1W_{i(01)}^{(\beta 1)} + \frac{1}{4}l_1^2W_{i(02)}^{(\beta 1)}]^{(q,r+1)} \quad (40)$$

where $i = 1, 2$, and 3 , which comprise the required additional 24 relations.

The equilibrium relations, Eqs. (32), together with the traction and displacement continuity conditions Eqs. (33)-(36) and (37)-(40), respectively, form 60 equations in the 60 unknowns $W_{i(mn)}^{(\beta\gamma)}$ which govern the

equilibrium of a subcell ($\beta\gamma$) within an interior cell (q, r); $q = 2, \dots, N_q - 1$, $r = 2, \dots, N_r - 1$. For the boundary cells $q = 1, N_q$ and $r = 1, N_r$ a different treatment must be applied.

For the boundary cell ($1, r$), the above relations are operative, except Eqs. (33) and (34), which follow from the continuity of tractions between a given cell and the preceding one (since cell ($0, r$) does not exist). These 12 equations must be replaced by the conditions of continuity of tractions at the interior interfaces within cell ($1, r$) (imposed in the average sense), and by the conditions that the fluctuating displacements are periodic. It follows, by employing the third set of relations in (15), that

$$[W_{i(00)}^{(1\gamma)} - \frac{1}{2}h_1 W_{i(10)}^{(1\gamma)} + \frac{1}{4}h_1^2 W_{i(20)}^{(1\gamma)}]^{(1,r)} = [W_{i(00)}^{(2\gamma)} + \frac{1}{2}h_2 W_{i(10)}^{(2\gamma)} + \frac{1}{4}h_2^2 W_{i(20)}^{(2\gamma)}]^{(N_q,r)} \quad (41)$$

where $i = 1, 2$, and 3 . Both conditions provide the required 12 relations to be used for cell ($1, r$).

For the boundary cell (N_q, r), the previously derived governing equations are operative except for the 6 relations given by Eqs. (38), which are obviously not applicable (since cell ($N_q + 1, r$) does not exist). These are replaced by the conditions that the tractions are periodic. Thus the first set of relations in (15), reproduced below for convenience, provides the 6 equations to be used for cell (N_q, r)

$$\int_{-l_\gamma/2}^{l_\gamma/2} \sigma_{2j}^{(1\gamma)} \Big|_{\bar{y}_2^{(1)} = -h_1/2}^{(1,r)} d\bar{y}_3^{(\gamma)} = \int_{-l_\gamma/2}^{l_\gamma/2} \sigma_{2j}^{(2\gamma)} \Big|_{\bar{y}_2^{(2)} = h_2/2}^{(N_q,r)} d\bar{y}_3^{(\gamma)} \quad (42)$$

where the stresses $\sigma_{ij}^{(\beta\gamma)}$ are given by Eq. (8).

Similar treatments hold for boundary cells ($q, 1$) and (q, N_r). Thus the 12 equations (35)-(36) are obviously not applicable in cell ($q, 1$) and should be replaced by the conditions of continuity of tractions at the interior interfaces within this cell (imposed in the average sense), and by the conditions that the fluctuating displacements are periodic. The latter yield according to the fourth set of relations in (15)

$$[W_{i(00)}^{(\beta 1)} - \frac{1}{2}l_1 W_{i(01)}^{(\beta 1)} + \frac{1}{4}l_1^2 W_{i(02)}^{(\beta 1)}]^{(q,1)} = [W_{i(00)}^{(\beta 2)} + \frac{1}{2}l_2 W_{i(01)}^{(\beta 2)} + \frac{1}{4}l_2^2 W_{i(02)}^{(\beta 2)}]^{(q,N_r)} \quad (43)$$

For the boundary cell (q, N_r), Eqs. (40) are not operative and they should be replaced by the periodicity of tractions which is given by the second set of relations in (15), reproduced below for convenience,

$$\int_{-h_\beta/2}^{h_\beta/2} \sigma_{3j}^{(\beta 1)} \Big|_{\bar{y}_3^{(1)} = -l_1/2}^{(q,1)} d\bar{y}_2^{(\beta)} = \int_{-h_\beta/2}^{h_\beta/2} \sigma_{3j}^{(\beta 2)} \Big|_{\bar{y}_3^{(2)} = l_2/2}^{(q,N_r)} d\bar{y}_2^{(\beta)} \quad (44)$$

Consequently, the governing equations for the interior and boundary cells form a system of $60N_qN_r$ algebraic equations in the unknown coefficients $W_{i(mn)}^{(\beta\gamma)}$. The final form of this system of equations can be symbolically represented by

$$\mathbf{KU} = \mathbf{f} + \mathbf{g} \quad (45)$$

where the structural stiffness matrix \mathbf{K} contains information on the geometry and thermomechanical properties of the materials within the individual subcells ($\beta\gamma$) of the cells comprising the multiphase periodic composite. The displacement vector \mathbf{U} contains the unknown displacement coefficients in each subcell, i.e.,

$$\mathbf{U} = [\mathbf{U}_{11}^{(11)}, \dots, \mathbf{U}_{N_q N_r}^{(22)}] \quad (46)$$

where in subcell ($\beta\gamma$) of cell (q, r) these coefficients are

$$\mathbf{U}_{qr}^{(\beta\gamma)} = [W_{i(00)}, W_{i(10)}, W_{i(01)}, W_{i(20)}, W_{i(02)}]_{qr}^{(\beta\gamma)} \quad i = 1, 2, 3$$

The mechanical force vector \mathbf{f} contains information on the applied average strains $\bar{\epsilon}_{ij}$ and the imposed temperature deviation ΔT , and the inelastic force vector \mathbf{g} appearing on the right-hand side of Eq. (45) contains the inelastic effects given in terms of the integrals of the inelastic stress distributions that are represented by the coefficients $R_{ij(m,n)}^{(\beta\gamma)}$. These integrals depend implicitly on the elements of the displacement coefficient vector \mathbf{U} , requiring an incremental procedure for the solution of Eq. (45) at each point along the loading path.

A careful check of the preceding equations reveals that the equations that govern the local normal and in-plane (2-3) shear deformations are coupled, thus providing the necessary shear coupling effects. On the other hand, these equations are not coupled to the axial shear deformations (1-2 and 1-3). Thus the above system, Eq. (45), can be decoupled in practical applications and solved for the normal and transverse shear deformations (with $40N_qN_r$ algebraic equations) separately from the axial shear deformations (with $20N_qN_r$ algebraic equations).

2.3 Global constitutive relations

Once the solution \mathbf{U} for a given set of average strains $\bar{\epsilon}$ has been established, we can determine, in particular, the average strains $[\mathbf{e}_{(0,0)}^{(\beta\gamma)}]^{(q,r)}$ in subcell $(\beta\gamma)$ of the cell (q, r) given by (18). The average stress components $[S_{ij(0,0)}^{(\beta\gamma)}]^{(q,r)}$ in subcell $(\beta\gamma)$ of the cell (q, r) are given by Eqs. (22), (25), (28) and (30). They can be assembled in a compact form as follows

$$[\mathbf{S}_{(0,0)}^{(\beta\gamma)}]^{(q,r)} = [\mathbf{C}^{(\beta\gamma)}\mathbf{e}_{(0,0)}^{(\beta\gamma)} - \mathbf{R}_{(0,0)}^{(\beta\gamma)} - \mathbf{\Gamma}^{(\beta\gamma)}\Delta T]^{(q,r)} \quad (47)$$

The equation relating the average total, plastic and thermal subcell strains, and macroscopically applied strains is obtained by generalizing the localization relation given in Aboudi *et al.* (2001) for elastic phases in the following manner

$$[\mathbf{e}_{(0,0)}^{(\beta\gamma)}]^{(q,r)} = [\mathbf{A}^{(\beta\gamma)}\bar{\epsilon} + \mathbf{D}^{(\beta\gamma)}]^{(q,r)} \quad (48)$$

where $[\mathbf{A}^{(\beta\gamma)}]^{(q,r)}$ is the mechanical strain concentration matrix of the subcell $(\beta\gamma)$, and $[\mathbf{D}^{(\beta\gamma)}]^{(q,r)}$ is a vector that involves current thermo-inelastic effects in the subcell. In the absence of thermal and inelastic effects this vector vanishes, and we can readily determine from (48) the mechanical strain concentration matrix $[\mathbf{A}^{(\beta\gamma)}]^{(q,r)}$ by solving the system (45) six consecutive times upon imposing a single non-zero component of $\bar{\epsilon}$ one at a time.

The thermo-inelastic analysis is performed in conjunction with an incremental procedure by imposing a spatially uniform temperature ΔT and the applied macroscopic strain $\bar{\epsilon}$ in a stepwise manner. Thus for a given value of applied thermomechanical loading, the average strains $[\mathbf{e}_{(0,0)}^{(\beta\gamma)}]^{(q,r)}$ in the subcell are obtained from the solution of Eq. (45), and hence the matrix $[\mathbf{D}^{(\beta\gamma)}]^{(q,r)}$ from (48) at the current loading level.

Substitution of (48) into (47) yields

$$[\mathbf{S}_{(0,0)}^{(\beta\gamma)}]^{(q,r)} = [\mathbf{C}^{(\beta\gamma)}(\mathbf{A}^{(\beta\gamma)}\bar{\epsilon} + \mathbf{D}^{(\beta\gamma)}) - \mathbf{R}_{(0,0)}^{(\beta\gamma)} - \mathbf{\Gamma}^{(\beta\gamma)}\Delta T]^{(q,r)} \quad (49)$$

The average stress in the multiphase periodic composite is determined from

$$\bar{\sigma} = \frac{1}{HL} \sum_{q=1}^{N_q} \sum_{r=1}^{N_r} \sum_{\beta,\gamma=1}^2 h_{\beta}^{(q)} l_{\gamma}^{(r)} [\mathbf{S}_{(0,0)}^{(\beta\gamma)}]^{(q,r)} \quad (50)$$

Consequently, Eqs. (49)-(50) establish the effective constitutive law of the multiphase thermo-elastic composite in the form

$$\bar{\sigma} = \mathbf{C}^* \bar{\epsilon} - (\bar{\sigma}^I + \bar{\sigma}^T) \quad (51)$$

where \mathbf{C}^* is the effective elastic stiffness matrix of the composite which is given by

$$\mathbf{C}^* = \frac{1}{HL} \sum_{q=1}^{N_q} \sum_{r=1}^{N_r} \sum_{\beta,\gamma=1}^2 h_{\beta}^{(q)} l_{\gamma}^{(r)} [\mathbf{C}^{(\beta\gamma)} \mathbf{A}^{(\beta\gamma)}]^{(q,r)} \quad (52)$$

and $\bar{\boldsymbol{\sigma}}^I$ and $\bar{\boldsymbol{\sigma}}^T$ denote the overall (macroscopic) inelastic and thermal stresses in the composite whose sum is given by

$$\bar{\boldsymbol{\sigma}}^I + \bar{\boldsymbol{\sigma}}^T = \frac{-1}{HL} \sum_{q=1}^{N_q} \sum_{r=1}^{N_r} \sum_{\beta,\gamma=1}^2 h_{\beta}^{(q)} l_{\gamma}^{(r)} [\mathbf{C}^{(\beta\gamma)} \mathbf{D}^{(\beta\gamma)} - \mathbf{R}_{(0,0)}^{(\beta\gamma)} - \mathbf{\Gamma}^{(\beta\gamma)} \Delta T]^{(q,r)} \quad (53)$$

Owing to the implicit dependence of $\mathbf{D}^{(\beta\gamma)}$ on the inelastic and thermal effects, the right hand side of (53) involves the combined inelastic and thermal contributions. It is very convenient to utilize the result obtained by Levin (1967) to separate the global inelastic and thermal effects. The global thermal stress in the multiphase composite $\bar{\boldsymbol{\sigma}}^T = \mathbf{\Gamma}^* \Delta T$ ($\mathbf{\Gamma}^*$ is related to the effective coefficients of thermal expansion $\boldsymbol{\alpha}^*$ of the composite by $\mathbf{\Gamma}^* = \mathbf{C}^* \boldsymbol{\alpha}^*$) is given in accordance with the Levin formula in terms of the mechanical strain concentration matrices and the thermal stress vector in the individual phases by

$$\bar{\boldsymbol{\sigma}}^T = \frac{\Delta T}{HL} \sum_{q=1}^{N_q} \sum_{r=1}^{N_r} \sum_{\beta,\gamma=1}^2 h_{\beta}^{(q)} l_{\gamma}^{(r)} [\mathbf{A}^{tr(\beta\gamma)} \mathbf{\Gamma}^{(\beta\gamma)}]^{(q,r)} \quad (54)$$

where $[\mathbf{A}^{tr(\beta\gamma)}]^{(q,r)}$ is the transpose of the mechanical strain concentration matrix $[\mathbf{A}^{(\beta\gamma)}]^{(q,r)}$ of subcell $(\beta\gamma)$ within cell (q,r) . This provides an additional check on the consistency of the proposed approach. Consequently, by utilizing Eq. (54) the overall inelastic stress of the composite can be readily obtained from (53), so that it can be represented in a closed-form manner, namely,

$$\bar{\boldsymbol{\sigma}}^I = \frac{-1}{HL} \sum_{q=1}^{N_q} \sum_{r=1}^{N_r} \sum_{\beta,\gamma=1}^2 h_{\beta}^{(q)} l_{\gamma}^{(r)} [\mathbf{C}^{(\beta\gamma)} \mathbf{D}^{(\beta\gamma)} - \mathbf{R}_{(0,0)}^{(\beta\gamma)} + (\mathbf{A}^{tr(\beta\gamma)} - \mathbf{I}) \mathbf{\Gamma}^{(\beta\gamma)} \Delta T]^{(q,r)} \quad (55)$$

We remark that, in the present framework, we have chosen to use the total formulation approximation of the field quantities which, in turn, results in the total form of the effective stress-strain relations for the multiphase material given by (51). The actual integration of the inelastic effects represented by the vector $[\mathbf{D}^{(\beta\gamma)}]^{(q,r)}$ depends on the chosen inelastic constitutive model for the individual phases. In the present paper, these effects are integrated using an iterative procedure within an incremental framework described in the next section for the incremental plasticity theory representation of the inelastic phase response. In the case of rate-dependent phase constitutive models, which the High-Fidelity Generalized Method of Cells' framework can naturally accomodate, either an explicit or an implicit integration scheme may be employed. This is in contrast with the approach employed by Paley and Aboudi (1992) where both total and rate formulations were employed in approximating the subcell field quantities. Similarly, rate formulations were employed by Fotiu and Nemat-Nasser (1996) and Walker *et al.* (1994). Chaboche *et al.* (2001) employed both rate (or tangential) and secant formulations in their extension of the Transformation Field Analysis which also included the presence of evolving damage modeled using the continuum damage mechanics approach. The present theoretical framework can also be reformulated in terms of rates, however for stand-alone applications there is no clear advantage of the total vs rate approach.

3 Numerical Results and Discussion

The focus of the extended High-Fidelity Generalized Method of Cells' validation is both the accurate prediction of the macroscopic inelastic response of a unidirectional metal matrix composite and the evolution of the local stress and inelastic strain fields at different macroscopic loading levels. The multiple concentric cylinder model, briefly described in the Appendix for completeness, is employed to validate the High-Fidelity Generalized Method of Cells' predictive capability under axisymmetric loading due to a spatially uniform temperature change (Pindera *et al.*, 1993), as well as under axial shear loading (Williams and Pindera 1997). This model is chosen because it provides fully analytical solutions for the local stress and inelastic strain fields, which satisfy the external boundary conditions together with the fiber/matrix interfacial displacement and traction continuity conditions under such loading. Therefore, these solutions are exact and provide the effective elastic and inelastic response of unidirectional composites with arbitrary fiber content. However, because the solutions are based on a particular geometry and the concept of a representative volume element which employs homogeneous boundary conditions to obtain solutions for the local fields, the functional form of the local fields is not affected by the presence of adjacent fibers. At dilute fiber volume fractions, the presence of adjacent fibers and the actual fiber array geometry has very little effect on both the local field quantities and the macroscopic response, and therefore the High-Fidelity Generalized Method of Cells which is based on periodicity (and the use of periodic rather than homogeneous boundary conditions) can be compared directly with the multiple concentric cylinder model predictions. This does not limit the generality of the conclusions obtained from such comparison due to the pronounced stress concentrations around the fiber/matrix interface, which give rise to the evolution of the local stress and inelastic strain fields whose complexity depends on the loading type. For instance, under axisymmetric loading, the inelastic strain field evolution depends only on the radial coordinate whereas under axial shear loading the angular dependence is also present, producing stress and inelastic strain fields that are two-dimensional. It is both the character and the magnitude of these local stress and inelastic strain fields for dilute fiber volume fractions that must be reproduced by the High-Fidelity Generalized Method of Cells, upon comparison with the multiple concentric cylinder model's predictions, that will validate the theory's predictive capability. Alternatively, at non-dilute fiber volume fractions, the presence of adjacent fibers will affect the local stress and inelastic strain fields. Therefore, the theory's predictions are expected to reflect this interaction relative to the multiple concentric cylinder model which does not directly account for the adjacent fibers' presence. Since the multiple concentric cylinder model cannot be used to generate a solution under transverse loading, the finite-element method was employed for this loading type to validate the theory's predictive capability.

Table 1. Elastic and thermal parameters of the transversely isotropic graphite fiber.

E_A (GPa)	ν_A	E_T (GPa)	ν_T	G_A (GPa)	α_A ($10^{-6}/^\circ\text{C}$)	α_T ($10^{-6}/^\circ\text{C}$)
388.20	0.41	7.60	0.45	14.90	-0.68	9.74

Table 2. Elastic, plastic and thermal parameters of the isotropic aluminum matrix.

E (GPa)	ν	G (GPa)	α ($10^{-6}/^\circ\text{C}$)	σ_y (MPa)	E_s (GPa)
72.40	0.33	27.22	22.5	286.67	11.70

A graphite/aluminum (gr/al) system is considered with the thermal, elastic and plastic moduli of the individual constituents given in Tables 1 and 2. The graphite fiber is linearly elastic and transversely isotropic, and the isotropic aluminum matrix is modeled using the classical incremental plasticity theory with isotropic

hardening. For this inelastic constitutive model, Mendelson's method of successive iterations described briefly below, and in detail elsewhere (Mendelson, 1986; Williams and Pindera, 1997), is employed to solve the system of equations (45) for the unknown coefficients $W_{i(mn)}^{(\beta\gamma)}$ and the plastic strain distributions $\epsilon_{ij}^{p(\beta\gamma)}$ in the individual subcells. Towards this end, the plastic strain field in the $(\beta\gamma)$ subcell at the current load level is expressed in terms of the known initial distribution from the preceding loading state plus an increment that results from the imposed load increment,

$$\epsilon_{ij}^{p(\beta\gamma)}(\bar{y}_2^{(\beta)}, \bar{y}_3^{(\gamma)})|_{current} = \epsilon_{ij}^{p(\beta\gamma)}(\bar{y}_2^{(\beta)}, \bar{y}_3^{(\gamma)})|_{previous} + d\epsilon_{ij}^{p(\beta\gamma)}(\bar{y}_2^{(\beta)}, \bar{y}_3^{(\gamma)}) \quad (56)$$

The plastic strain increments at the individual locations within the subcell are calculated using the Prandtl-Reuss flow rule expressed in terms of so-called modified total strain deviators e'_{ij} , rather than deviatoric stresses, as follows (omitting the superscript $(\beta\gamma)$ for notational clarity)

$$d\epsilon_{ij}^p = \frac{e'_{ij}}{\bar{e}_{eff}} d\bar{\epsilon}^p \quad (57)$$

where $e'_{ij} = \epsilon_{ij} - 1/3\epsilon_{kk}\delta_{ij} - \epsilon_{ij}^p|_{previous}$, $\bar{e}_{eff} = \sqrt{2/3e'_{ij}e'_{ij}}$, and the effective plastic strain increment $d\bar{\epsilon}^p$ is

$$d\bar{\epsilon}^p = \bar{e}_{eff} - \bar{\sigma}/3\mu \quad (58)$$

where μ is the shear modulus.

Without loss of generality in validating the theory's predictive capability, we take the elastoplastic response of the aluminum matrix to be bilinear, with the effective stress $\bar{\sigma}(\bar{\epsilon}^p)$ given by

$$\bar{\sigma}(\bar{\epsilon}^p) = \sigma_y + H_p \bar{\epsilon}^p \quad (59)$$

where σ_y is the yield stress in simple tension, and H_p is the slope of the effective stress-plastic strain curve, related to the secondary modulus E_s in the bilinear stress-strain representation of the elastoplastic response (see Table 2) as follows

$$H_p = \frac{EE_s}{E - E_s} \quad (60)$$

where E is the Young's modulus of the isotropic aluminum.

The above form of the incremental plasticity equations is completely equivalent to the classical one, but has the added advantage of producing very quick convergence when used in conjunction with Mendelson's iterative scheme for the solution of Eq. (45), as demonstrated in our previous investigations. The implementation of these equations is facilitated by the following loading condition for plastic loading

$$1 - \frac{\bar{\sigma}}{3\mu\bar{e}_{eff}} > 0 \quad (61)$$

shown previously to produce very fast convergence.

The fiber volume fractions (v_f) of the gr/al composite employed in the validation studies are 0.05 and 0.25, respectively, which henceforth will be referred to as dilute and non-dilute fiber volume fractions. Figure 3 shows the volume discretizations of the repeating unit cell for these two cases. In both cases, the unit cells contain 36×36 subcells appropriately dimensioned to approximate the circular fiber shape with sufficient accuracy. This was accomplished using a commercial optimization code.

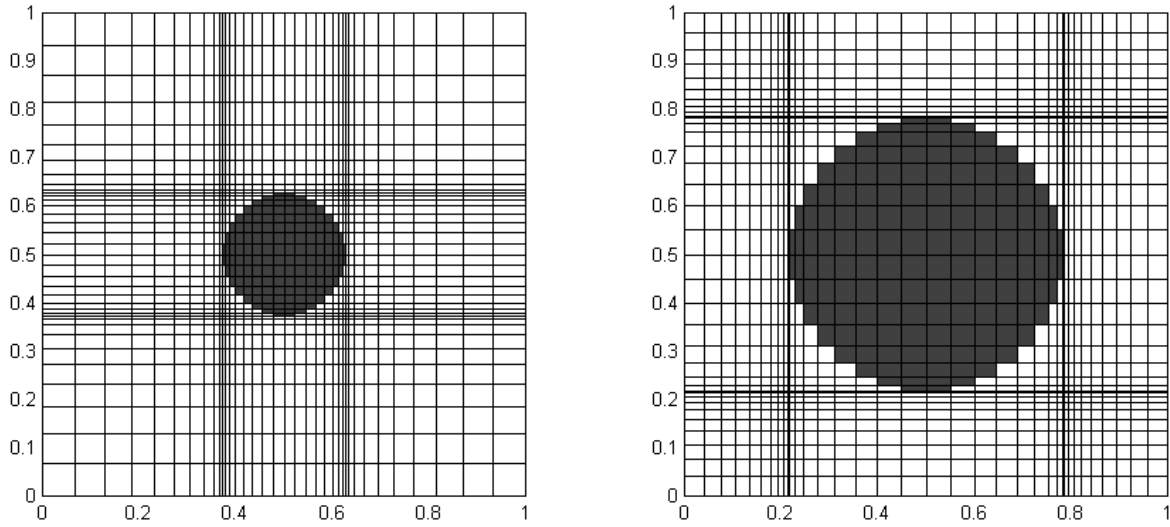


Figure 3. Volume discretization of the repeating unit cells employed in the analysis of unidirectional fiber-reinforced, metal-matrix composites: (left) $v_f = 0.05$; (right) $v_f = 0.25$.

3.1 Axisymmetric thermal loading

As the first step, we compare the predictions of the High-Fidelity Generalized Method of Cells and the multiple concentric cylinder model for the thermal response of the gr/al unidirectional composite during spatially uniform cooldown from 500° C to 25° C. This is the simplest case which results in axisymmetric displacement, stress and (plastic) strain fields within the individual phases of the multiple concentric cylinder model. As is well-known, the macroscopic axial response for this loading case can be predicted with good accuracy by the simplest micromechanics models irrespective of the fiber volume fraction. Thus a true test of the theory's predictive capability is the evolution of the plastic strain field in the aluminum phase as a function of temperature, which should retain an axisymmetric character for the dilute (i.e., noninteracting) fiber volume fraction composite. This is the focus of this section.

Figure 4 presents the macroscopic axial and transverse response of the gr/al unidirectional composite with the two fiber volume fractions as a function of temperature generated by the two models, which provides information on the initiation of yielding in the aluminum phase. For the dilute fiber volume fraction composite, Fig. 4(top), yielding initiates slightly above 300° C, while in the non-dilute case this occurs at around 250° C, Fig. 4(bottom). In order to obtain initiation of yielding for the two cases at comparable temperature levels when cooled from a common temperature, the yield stress of the aluminum phase in the dilute fiber volume fraction composite was taken to be one fourth of the yield stress employed in the non-dilute fiber volume fraction composite reported in Table 2.

As expected, both models predict virtually identical macroscopic thermal response in the axial direction for the dilute and non-dilute fiber volume fraction cases. The same observation holds true for the effective transverse response. Based on the macroscopic thermal response shown in Fig. 4(top), the effective plastic strain distributions for the dilute fiber volume fraction composite have been generated at 300°, 200° and 25° C using the High-Fidelity Generalized Method of Cells and the multiple concentric cylinder model. The effective plastic strain distributions are calculated by integrating the effective plastic strain increment $d\bar{\epsilon}^P$ at

each load increment along the entire loading history at the particular point, i.e.,

$$\bar{\varepsilon}^P = \int d\bar{\varepsilon}^P$$

where $d\bar{\varepsilon}^P$ is given by Eq. (58). These distributions are shown in Fig. 5. In this dilute fiber volume fraction case, little interaction is expected between adjacent fibers in the periodic square fiber array model employed in the High-Fidelity Generalized Method of Cells. Thus the character of the effective plastic strain distribution in the aluminum phase predicted by this model should be essentially axisymmetric and therefore comparable to that predicted by the multiple concentric cylinder model. This is indeed the case with respect to both the distribution as well as the magnitude, as observed in Fig. 5. It is remarkable that the magnitude of the effective plastic strain field is predicted with high accuracy by the High-Fidelity Generalized Method of Cells even during the initial stages of yield initiation at 300° C shown in the top portion of Fig. 5. This demonstrates that the method is sufficiently sensitive to capture accurately the plastic strain field even when the effective plastic strain magnitudes are very small.

In the case of the non-dilute fiber volume fraction composite, the effective plastic strain distributions have been generated at 200°, 100° and 25° C, based on the macroscopic thermal response given in Fig. 4(bottom). These distributions are shown in Fig. 6. During the initial stages of yield initiation, the effective plastic strain distribution predicted by the High-Fidelity Generalized Method of Cells at 200° C retains an axisymmetric character and compares favorably with the multiple concentric cylinder model prediction. The interaction with adjacent fibers becomes apparent at the lower temperatures as the magnitude of the effective plastic strain predicted by the high-fidelity model within the plastic zone increases, losing its axisymmetric character away from the fiber. In the immediate vicinity of the fiber/matrix interface, however, the axisymmetric character of the effective plastic strain distribution is preserved and compares very well in magnitude with the multiple concentric model prediction.

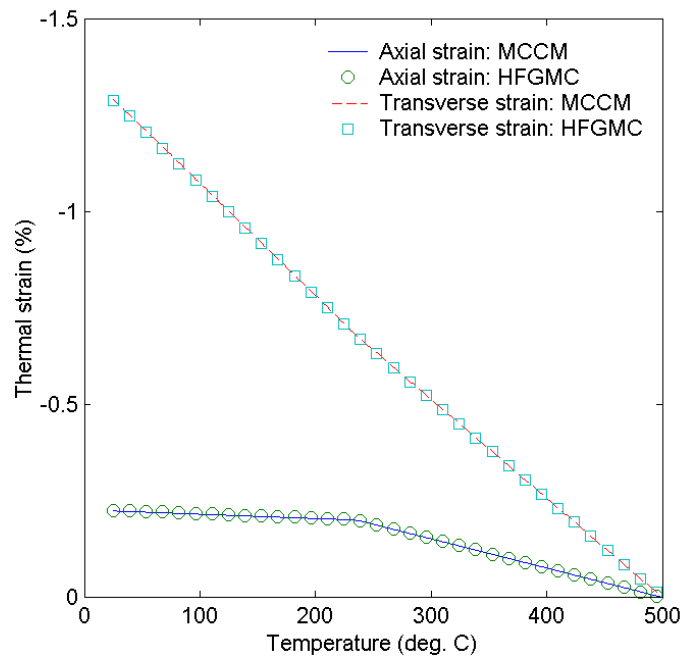
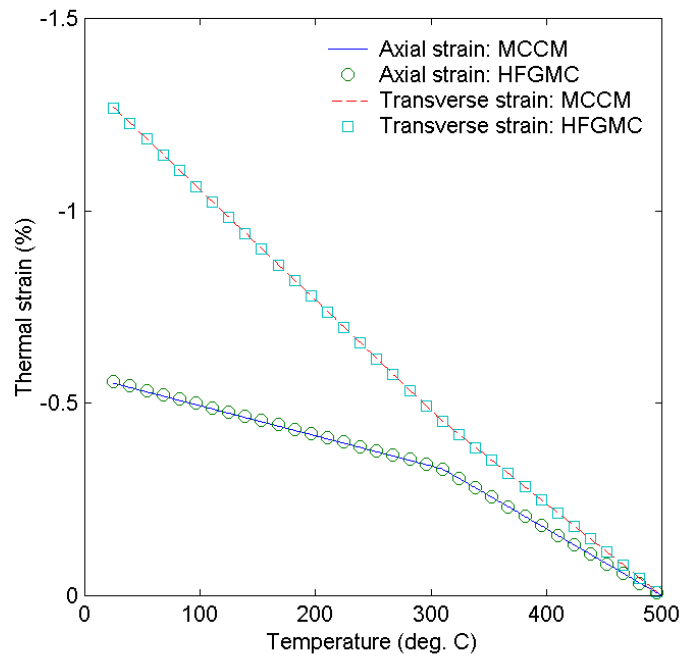


Figure 4. Macroscopic thermal response of a unidirectional gr/al composite during spatially uniform cooldown from 500° C to 25° C: (top) $v_f = 0.05$; (bottom) $v_f = 0.25$. (Note that for $v_f = 0.05$, an altered matrix yield stress, $\sigma_y = 286.67/4$ MPa was employed, see Table 2).

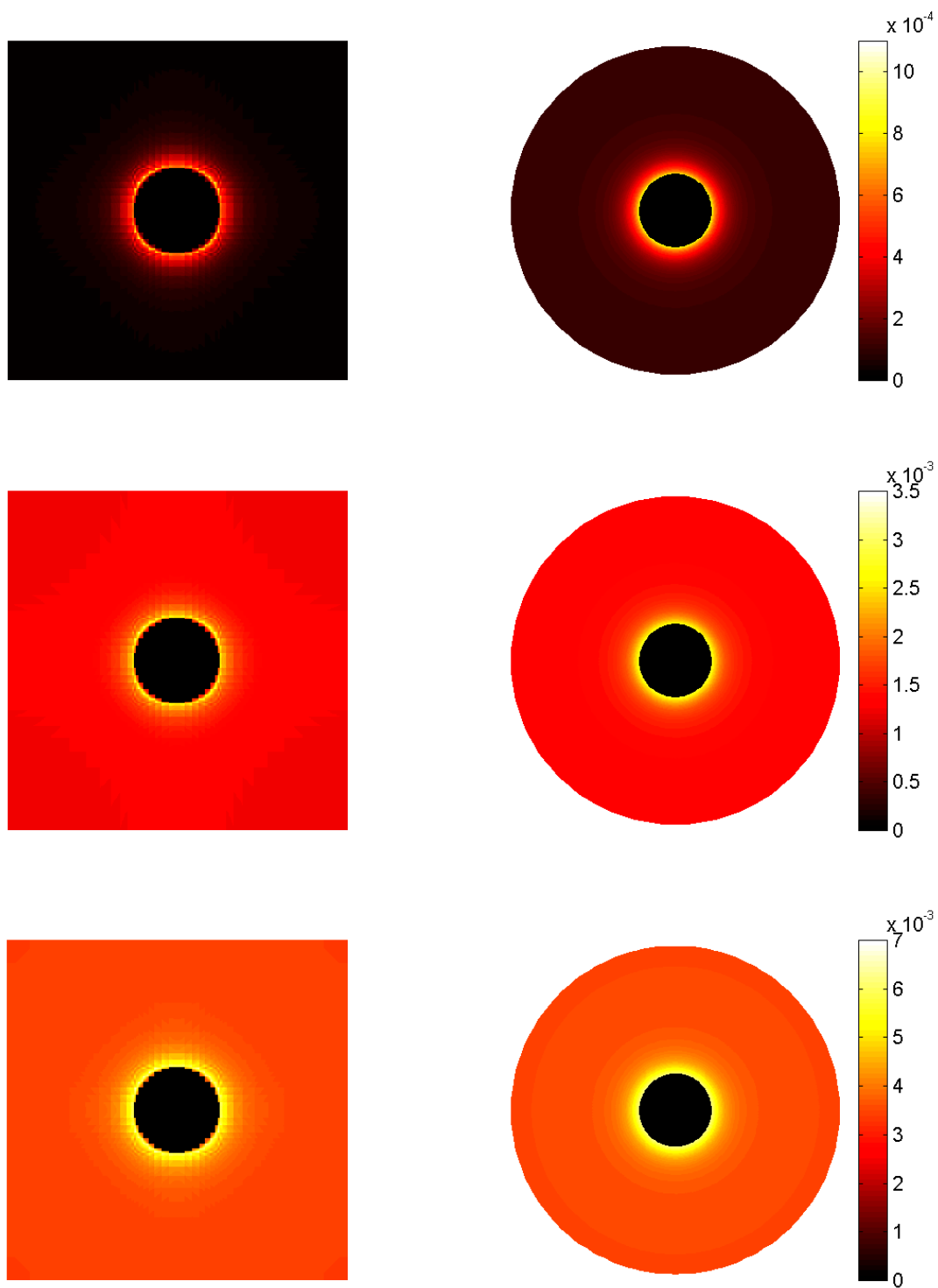


Figure 5. Effective plastic strain distributions in the aluminum phase of a unidirectional gr/al composite with $v_f = 0.05$, cooled from 500° C, at 300° C (top), 200° C (middle), and 25° C (bottom). Comparison of the High-Fidelity Generalized Method of Cells predictions (left column) with the multiple concentric cylinder results (right column).

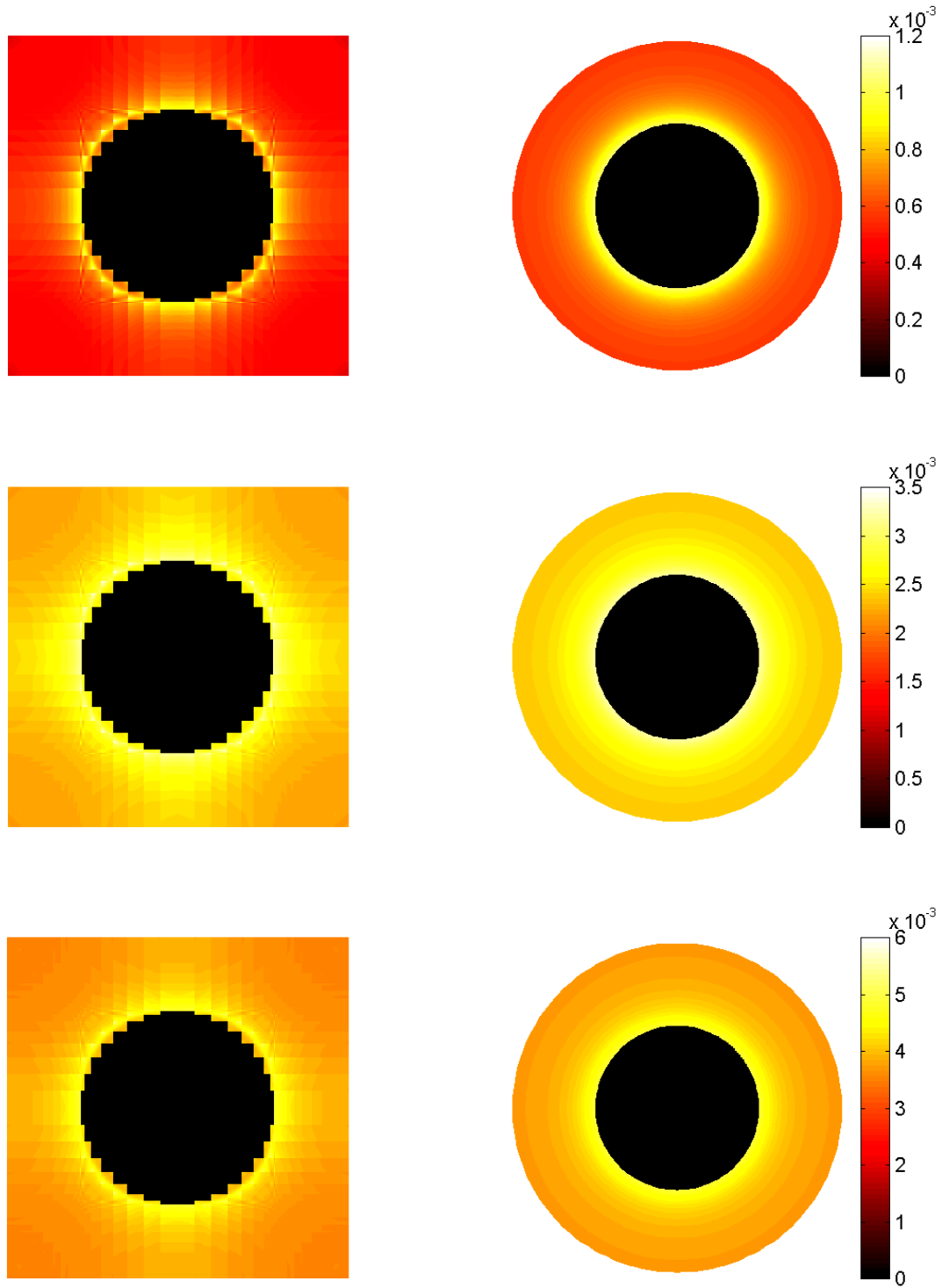


Figure 6. Effective plastic strain distributions in the aluminum phase of a unidirectional gr/al composite with $v_f = 0.25$, cooled from 500°C , at 200°C (top), 100°C (middle), and 25°C (bottom). Comparison of the High-Fidelity Generalized Method of Cells predictions (left column) with the multiple concentric cylinder results (right column).

3.2 Axial shear loading

In comparing the predictions of both models for the axial shear loading case in the $x_1 - x_3$ plane (see Fig. 1), the following features of the local stress fields should be kept in mind. For the dilute fiber volume fraction composite in the elastic region, the σ_{13} shear stress distribution in the fiber region obtained from the multiple concentric cylinder model is uniform while the σ_{12} shear stress is zero. The evolution of plastic deformation in the matrix phase introduces slight nonuniformities in these distributions. This is also true in the non-dilute case since this model does not account directly for the interaction due to adjacent fibers. Further, the σ_{13} shear stress distribution is symmetric with respect to the horizontal and vertical planes through the fiber's center, while the σ_{12} shear stress distribution is antisymmetric irrespective of the fiber volume fraction at all loading levels. With the exception of the interaction effect due to adjacent fibers in the non-dilute case, the above features of the local stress fields must be captured by the High-Fidelity Generalized Method of Cells.

We start by presenting the macroscopic shear stress-strain predictions of the two models due to shearing by the applied average strain $\bar{\epsilon}_{13}$. These responses are given in Fig. 7 for both the dilute and non-dilute cases, and form the basis for the microscopic stress and effective plastic strain distributions presented at different applied shear strain levels in the subsequent figures. In generating the shear response, the properties of the aluminum matrix given in Table 2 were employed while the fiber was assumed to be isotropic with the shear modulus $G = 137.7$ GPa, following Williams and Pindera (1997). This produces a fiber/matrix shear modulus ratio of approximately 5, which provides a greater property mismatch than that obtained using the properties of the transversely isotropic graphite fiber given in Table 1.

In the case of the dilute fiber volume fraction composite, Fig. 7(top), the predictions of the High-Fidelity Generalized Method of Cells and the multiple concentric cylinder model are identical in both the elastic and elastoplastic region, with macroscopic yielding occurring around $\bar{\epsilon}_{13} = 0.3\%$. Based on the observed macroscopic response, the microscopic stress distributions are given at $\bar{\epsilon}_{13} = 0.1, 0.5$, and 0.75% , while the microscopic effective plastic strain distributions are given at $\bar{\epsilon}_{13} = 0.3, 0.5$, and 0.75% . The elastic shear stress distributions at $\bar{\epsilon}_{13} = 0.1\%$ are included because the character of the microscopic stress field is affected by the growth of the plastic zone in the aluminum matrix even at low fiber volume fractions, unlike the axisymmetric thermal loading case discussed in the previous section. In the case of the non-dilute fiber volume fraction composite, Fig. 7(bottom), the predictions of the High-Fidelity Generalized Method of Cells and the multiple concentric cylinder model are also identical in the elastic region, with macroscopic yielding occurring around $\bar{\epsilon}_{13} = 0.225\%$. In the elastoplastic region, the macroscopic shear response predicted by the High-Fidelity Generalized Method of Cell is slightly lower relative to the multiple concentric cylinder model prediction, indicating that the interaction with adjacent fibers is becoming noticeable. Based on the observed macroscopic response, the microscopic stress distributions are given at $\bar{\epsilon}_{13} = 0.1, 0.5$, and 0.75% as in the dilute case, while the microscopic effective plastic strain distributions are given at $\bar{\epsilon}_{13} = 0.25, 0.5$, and 0.75% .

The microscopic shear stress σ_{13} distributions predicted by the High-Fidelity Generalized Method of Cells and the multiple concentric cylinder model for the dilute case are compared in Fig. 8 at the given applied shear strain levels. Both the character and the magnitude of the local shear stress field is captured with very good accuracy by the high-fidelity model in this dilute case, including the initially nearly uniform shear stress distribution in the fiber and the highly nonuniform distribution in the matrix phase in the elastic region, and the effect of matrix plasticity on these distributions with progressive loading. Of particular significance is the symmetry of the σ_{13} field with respect to the horizontal and vertical planes through the fiber's center during all stages of loading. The effect of plasticity on the character of the shear stress field is also dramatic, and perhaps more apparent, in the case of the σ_{12} distributions presented in Fig. 9 due to the antisymmetric character of the stress field with respect to the horizontal and vertical planes. In this case, yielding of the matrix phase skews the σ_{12} distributions away from the bisectors of the horizontal and vertical axes through the fiber's center towards the vertical axis as observed in the middle and bottom

portions of Fig. 9. This phenomenon is very well captured by the High-Fidelity Generalized Method of Cells, as is the perfect antisymmetry of the σ_{12} field with respect to the horizontal and vertical planes. As in the preceding case, the magnitude of the σ_{12} field predicted by the high-fidelity model compares very well with the multiple concentric cylinder model prediction at the three applied shear strain levels. It is therefore not surprising that the effective plastic strain distributions predicted by the high-fidelity model also compare very well with the multiple concentric cylinder model predictions both in character and magnitude, as observed in Fig. 10. This is true even during the early stages of yield initiation when the effective plastic strain magnitudes are very small.

In the non-dilute case, the effect of adjacent fibers on the microscopic shear stress fields generated by the High-Fidelity Generalized Method of Cells becomes apparent. The magnitude of this effect depends on the particular shear stress component and the extent of plastic deformation. In the case of the shear stress σ_{13} distributions shown in Fig. 11, the shear stress in the fiber is nearly uniform in the elastic region and compares very well in magnitude with the multiple concentric cylinder model result (Fig. 11(top)). The matrix shear stress field is also well captured by the high-fidelity model. As the extent of the plastic zone grows, the interaction with adjacent fibers becomes more apparent both in the fiber and the matrix phases. Specifically, the high-fidelity model predicts greater extent of the fiber shear stress nonuniformity, and a smaller shear stress gradient in the matrix phase in the plane of shearing, relative to the multiple concentric cylinder results.

In the case of the shear stress σ_{12} distributions shown in Fig. 12, the shear stress in the fiber becomes nonuniform already in the elastic region. However, the basic character and magnitude of the shear stress field is essentially the same as that predicted by the multiple concentric cylinder model. As in the dilute case, plastic deformation in the matrix phase skews the shear stress field away from the bisectors of the horizontal and vertical axes through the fiber's center towards the vertical axis, albeit not to the same extent as in the dilute case and as predicted by the multiple concentric cylinder model. In general, in the non-dilute case the overall character of the shear stress σ_{12} distributions in the elastoplastic region better resembles the corresponding multiple concentric cylinder model predictions than does the character of the σ_{13} distributions.

The influence of adjacent fibers in the periodic array model employed by the High-Fidelity Generalized Method of Cells is also apparent in the effective plastic strain distributions shown in Fig. 13 for the non-dilute case. During the initial stages of yielding, this influence is not noticeable (Fig. 13(top)), but increases at the higher levels of deformation (Fig. 13(middle and bottom)). Specifically, the constraint due to the adjacent fibers retards the growth of the plastic zone in the matrix phase in the direction normal to the plane of shearing, and enhances it in the shearing plane itself. In the immediate vicinity of the fiber/matrix interface, however, both the character and magnitude of the effective plastic strain field predicted by the high-fidelity model compare very well with the multiple concentric cylinder model prediction.

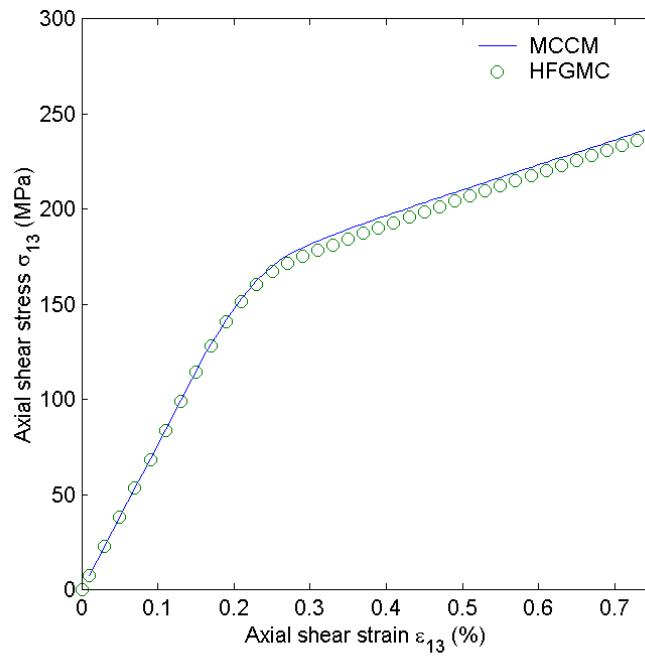
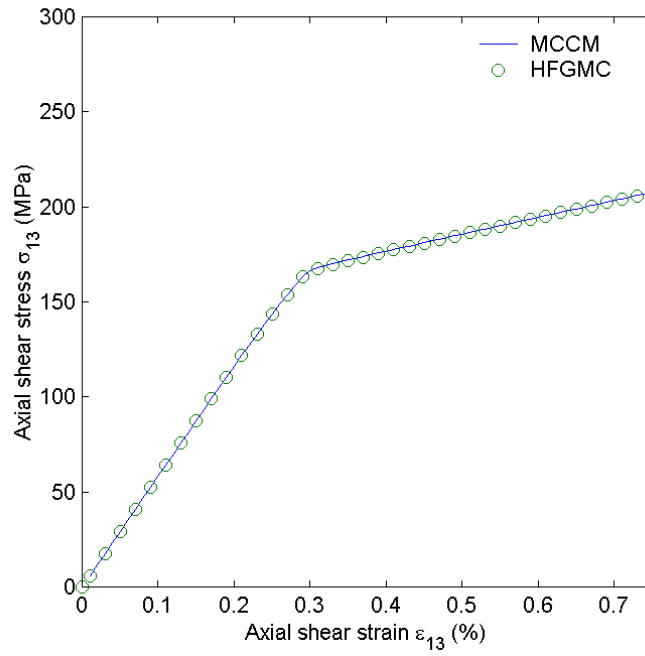


Figure 7. Macroscopic shear stress-strain response, $\bar{\sigma}_{13}$ vs $\bar{\epsilon}_{13}$, of a unidirectional gr/al composite due to shearing in the $x_1 - x_3$ plane: (top) $v_f = 0.05$; (bottom) $v_f = 0.25$. Comparison of the High-Fidelity Generalized Method of Cells predictions with the multiple concentric cylinder model results. (Note that in this case the graphite fiber is treated as isotropic with $G = 137.7$ GPa).

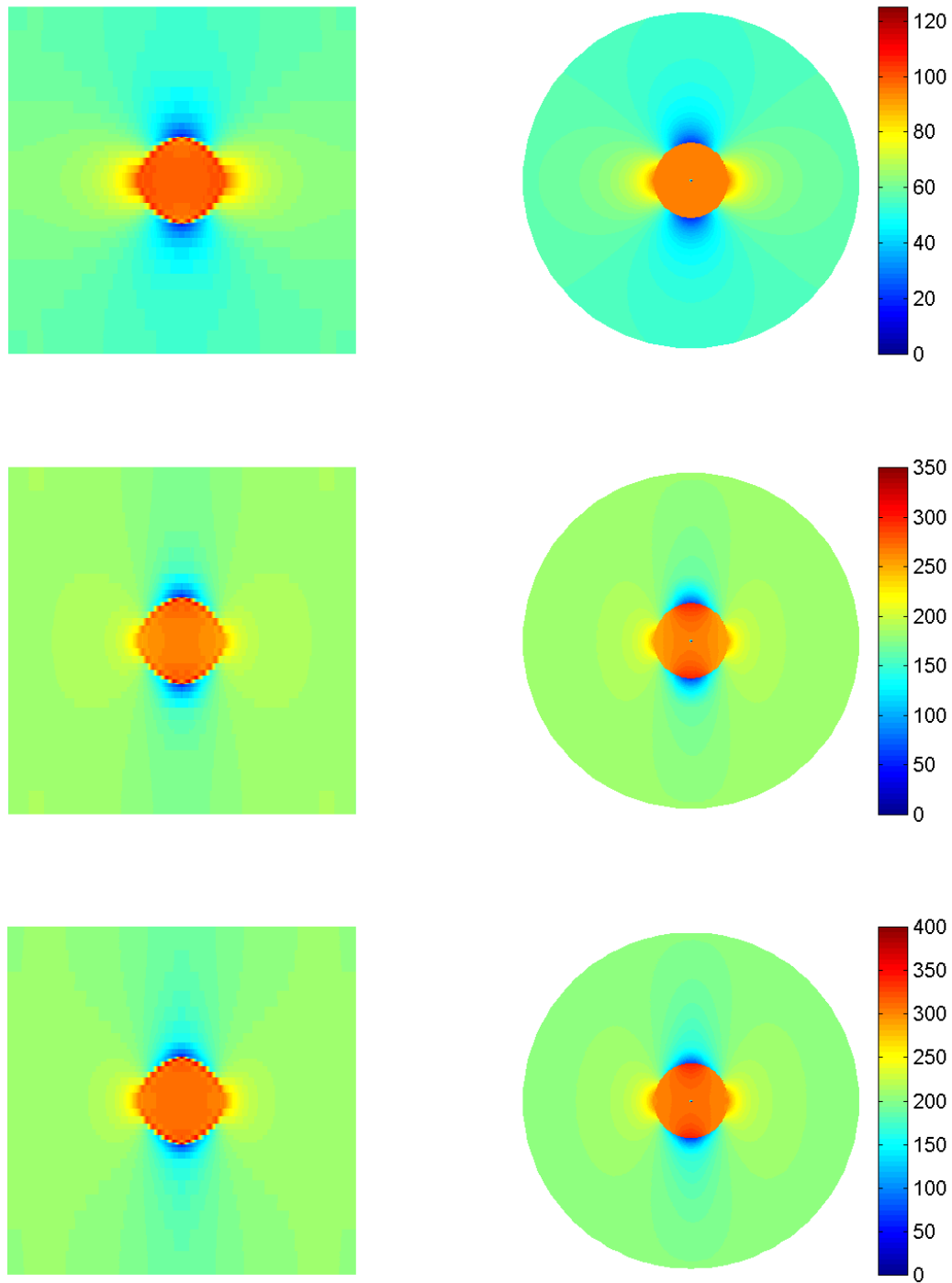


Figure 8. Shear stress σ_{13} distributions in the individual phases of a unidirectional gr/al composite with $v_f = 0.05$ at the applied average shear strain $\bar{\epsilon}_{13}$ of 0.1% (top), 0.5% (middle), and 0.75% (bottom). Comparison of the High-Fidelity Generalized Method of Cells predictions (left column) with the multiple concentric cylinder results (right column). Colorbar in MPa. (Note that the dot at the fiber's center is a plotting artifact).

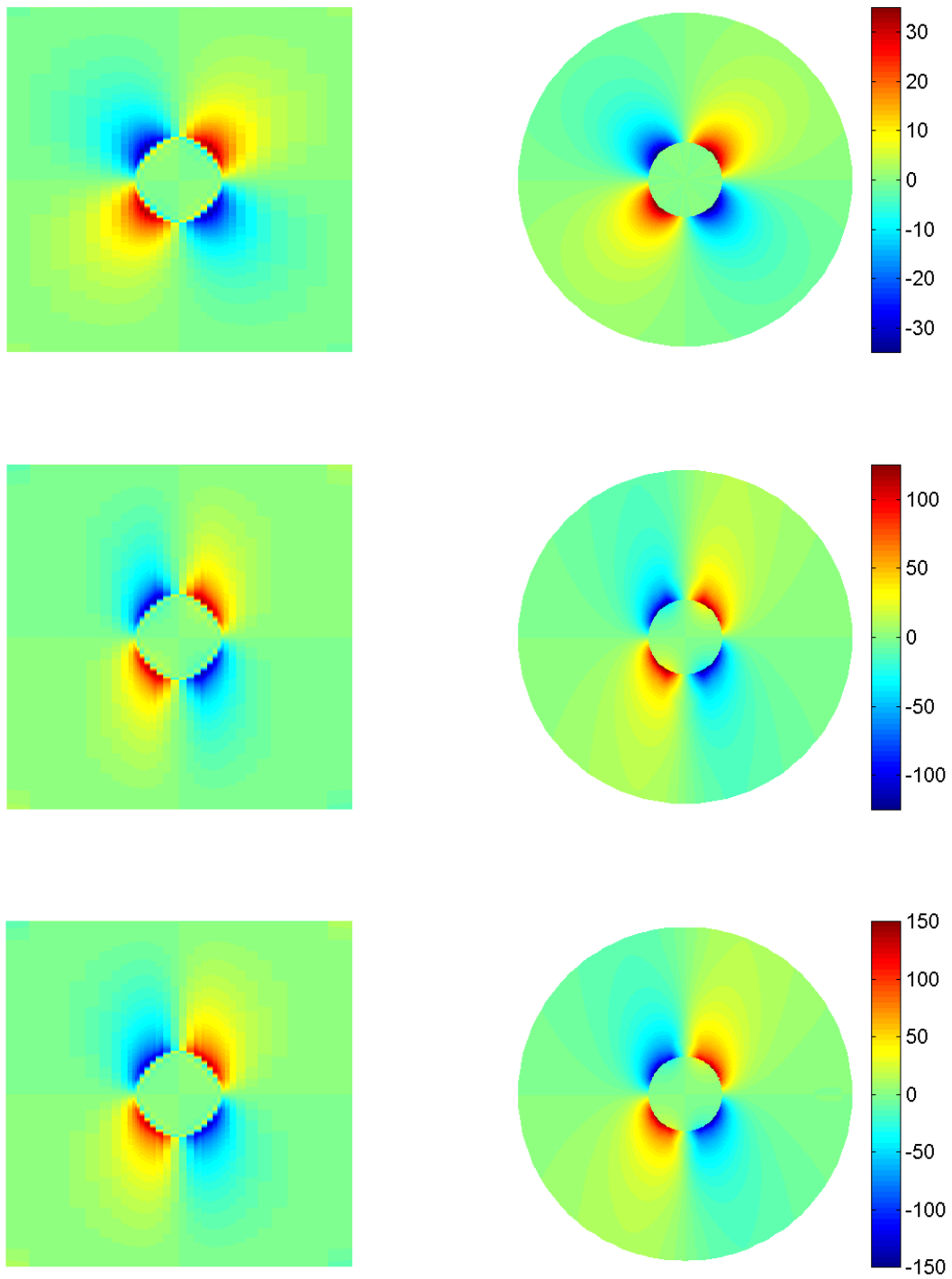


Figure 9. Shear stress σ_{12} distributions in the individual phases of a unidirectional gr/al composite with $v_f = 0.05$ at the applied average shear strain $\bar{\epsilon}_{13}$ of 0.1% (top), 0.5% (middle), and 0.75% (bottom). Comparison of the High-Fidelity Generalized Method of Cells predictions (left column) with the multiple concentric cylinder results (right column). Colorbar in MPa.

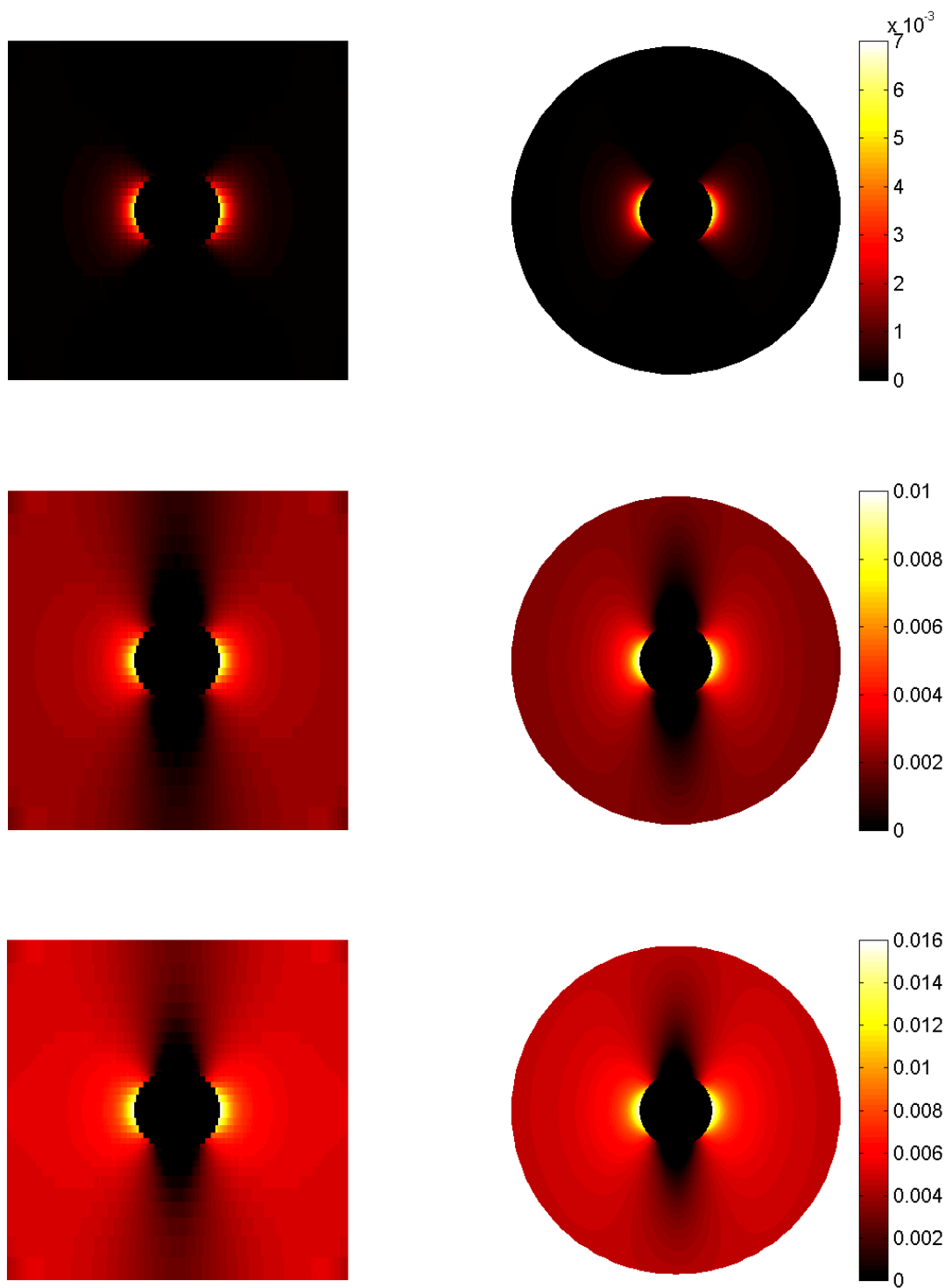


Figure 10. Effective plastic strain distributions in the aluminum phase of a unidirectional gr/al composite with $v_f = 0.05$ at the applied average shear strain $\bar{\epsilon}_{13}$ of 0.3% (top), 0.5% (middle), and 0.75% (bottom). Comparison of the High-Fidelity Generalized Method of Cells predictions (left column) with the multiple concentric cylinder results (right column).

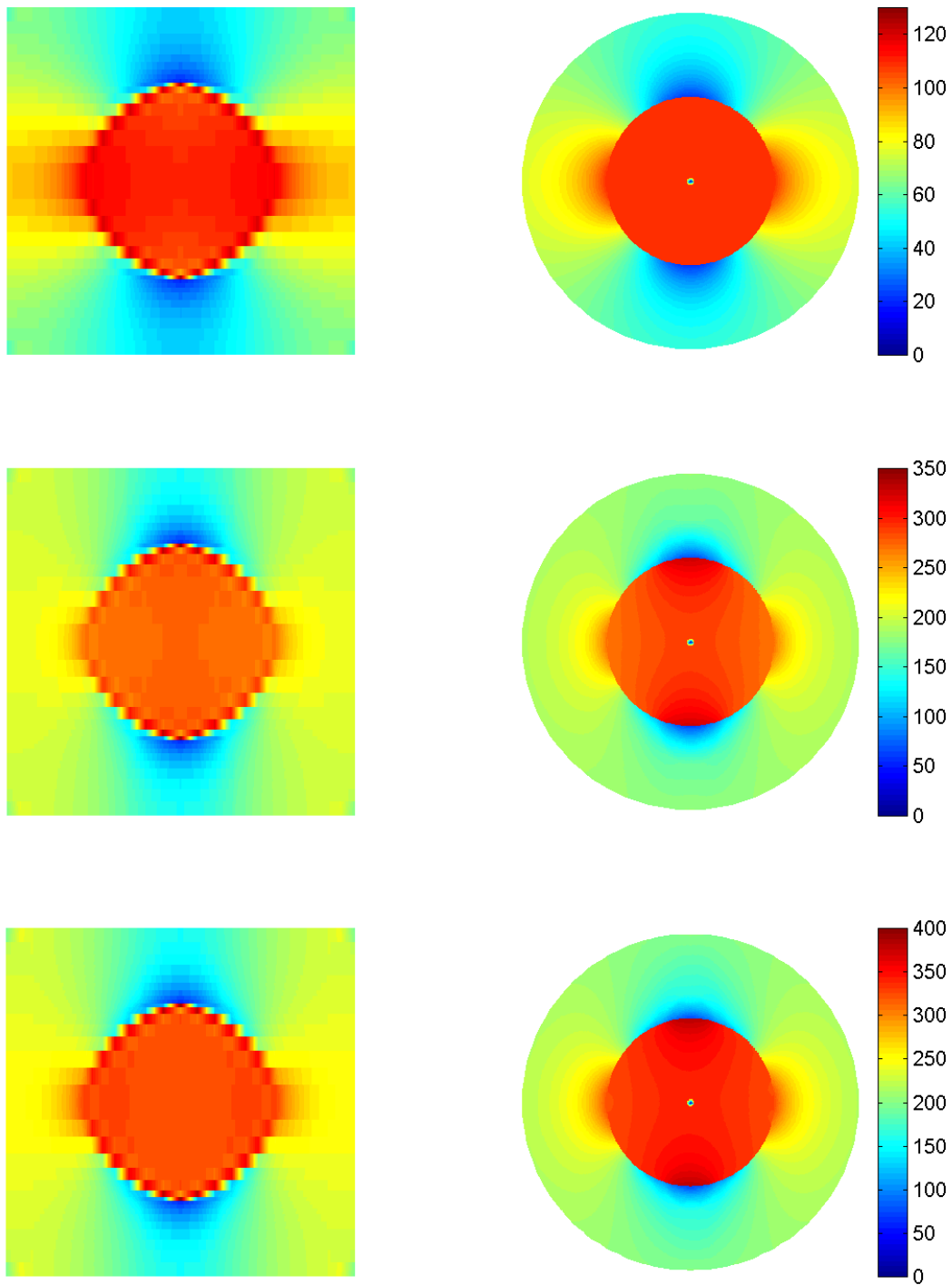


Figure 11. Shear stress σ_{13} distributions in the individual phases of a unidirectional gr/al composite with $v_f = 0.25$ at the applied average shear strain $\bar{\epsilon}_{13}$ of 0.1% (top), 0.5% (middle), and 0.75% (bottom). Comparison of the High-Fidelity Generalized Method of Cells predictions (left column) with the multiple concentric cylinder results (right column). Colorbar in MPa. (Note that the dot at the fiber's center is a plotting artifact).

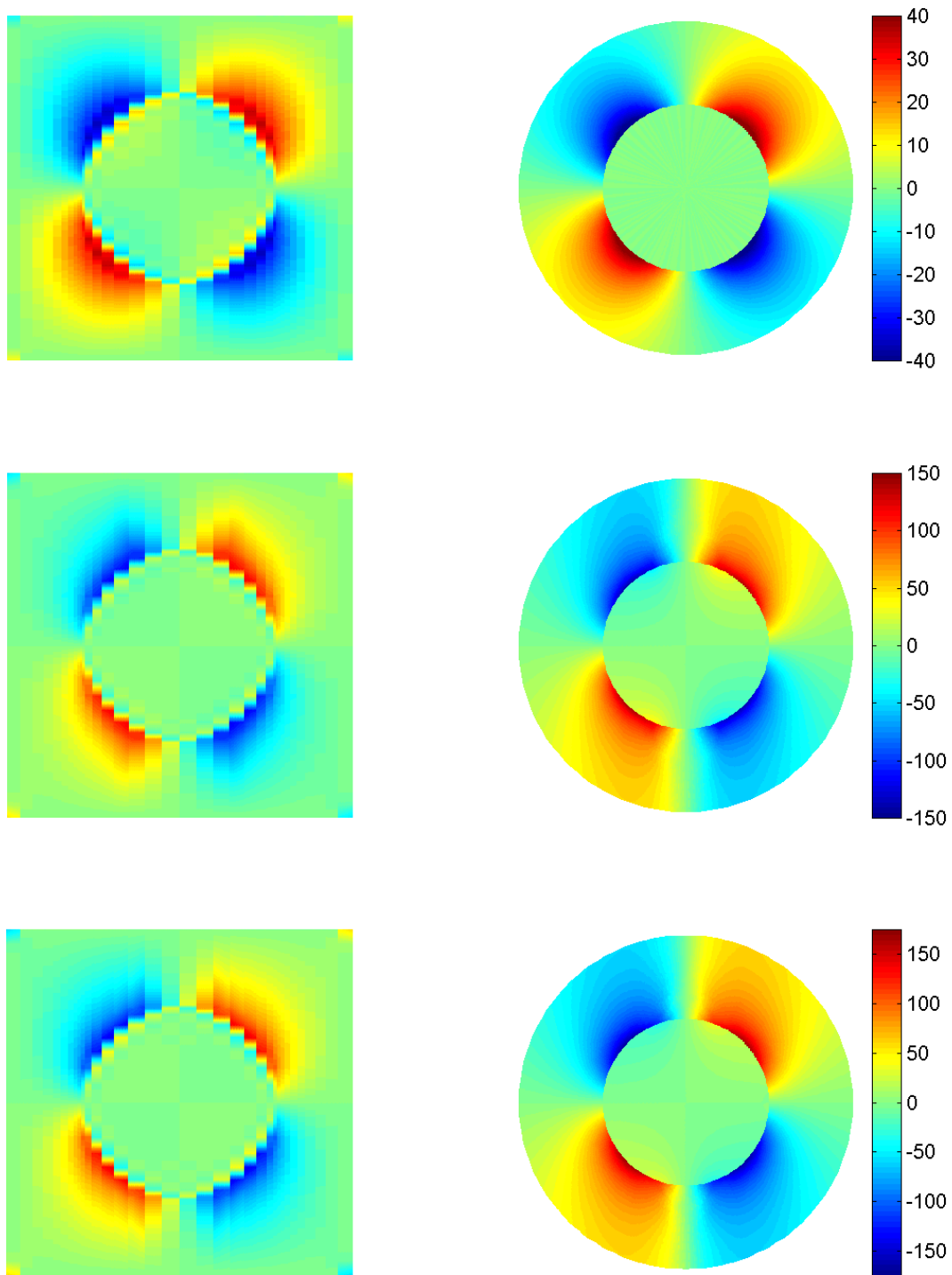


Figure 12. Shear stress σ_{12} distributions in the individual phases of a unidirectional gr/al composite with $v_f = 0.25$ at the applied average shear strain $\bar{\epsilon}_{13}$ of 0.1% (top), 0.5% (middle), and 0.75% (bottom). Comparison of the High-Fidelity Generalized Method of Cells predictions (left column) with the multiple concentric cylinder results (right column). Colorbar in MPa.

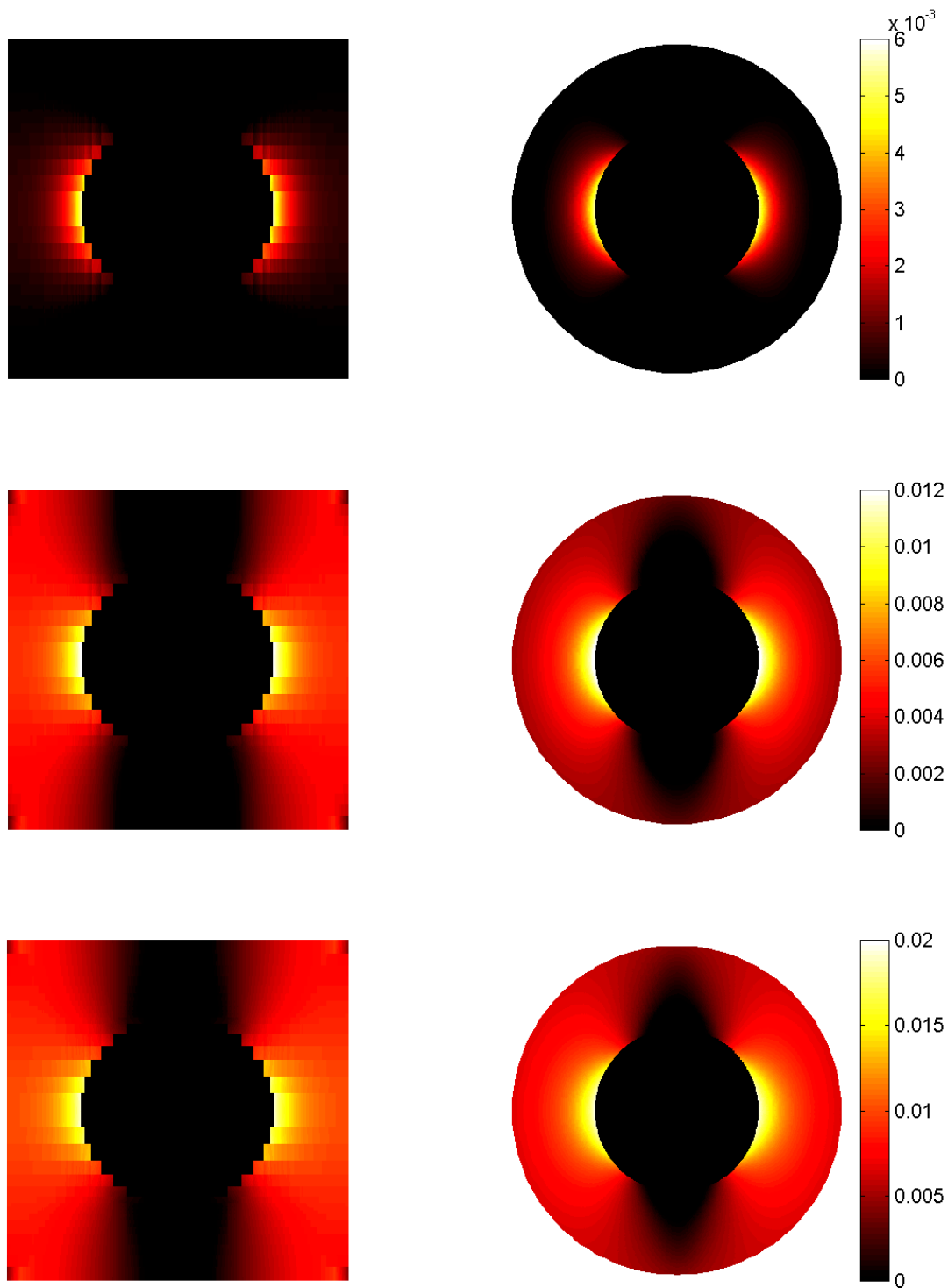


Figure 13. Effective plastic strain distributions in the aluminum phase of a unidirectional gr/al composite with $v_f = 0.25$ at the applied average shear strain $\bar{\epsilon}_{13}$ of 0.3% (top), 0.5% (middle), and 0.75% (bottom). Comparison of the High-Fidelity Generalized Method of Cells predictions (left column) with the multiple concentric cylinder results (right column).

3.3 Transverse normal loading

The commercial finite-element program ANSYS was employed to generate the response of the gr/al unidirectional composite under transverse loading. Refined representations of the repeating unit cell containing 1,782 elements with 4,989 nodes for the dilute case, and 1,260 elements with 3,909 nodes for the non-dilute case, were constructed using 8-noded, plane-strain quadrilateral elements. External loading was specified in the form of uniform displacements of opposite signs but equal magnitudes applied to the horizontal and vertical boundaries of the unit cell under the condition of plane strain in the out-of-plane direction. This type of loading represents pure shearing in the coordinate system rotated by 45° about the fiber's center, and provides a critical test of the High-Fidelity Generalized Method of Cells' predictive capabilities under transverse loading. In the context of the finite-element analysis, it also eliminates the need for an iterative solution procedure when transverse loading is applied in just one direction in order to ensure that the average stress in the other direction remains zero. The same loading was employed to generate the High-Fidelity Generalized Method of Cells results (i.e., $\bar{\epsilon}_{22} = -\bar{\epsilon}_{33}$ with $\bar{\epsilon}_{11} = 0$).

For this loading case, the actual properties of the transversely isotropic graphite fiber were employed in the calculations. Therefore, the matrix is 3.58 times stiffer than the fiber in the loading plane (see Tables 1 and 2), in contrast with the axial shearing case where the fiber was approximately 5 times stiffer than the matrix in the plane of shearing. The smaller transverse stiffness of the fiber relative to the matrix in the present case is expected to produce substantially different trends than those observed in the axial shearing case both at the macroscopic and microscopic scales, providing a completely different test for the High-Fidelity Generalized Method of Cells' predictive capability. This is indeed the case as demonstrated first in Fig. 14 which provides the comparison between the high-fidelity model and finite-element predictions of the macroscopic stress-strain response for the two fiber volume fraction composites. Specifically, the stress-strain response for the non-dilute case is lower relative to the dilute case. Further, there is virtually no difference between the predictions of the two models for the two cases.

Included in Fig. 14 are the corresponding predictions of the original Generalized Method of Cells for the two fiber fraction cases. As observed, the initial elastic response is very well captured by the Generalized Method of Cells despite the inherent absence of shear coupling in this simpler micromechanical model. The predictive capability of this model is also quite good in the elastoplastic region, but does depend on the fiber volume fraction as expected. The reason for the original Generalized Method of Cells' ability to model the macroscopic inelastic response of metal matrix composites with good accuracy will become apparent upon examination of the internal stress fields.

Based on the macroscopic stress-strain curves, local field quantities were generated at the applied $\bar{\epsilon}_{33}$ strain levels of 0.4 and 1.0%. Figure 15 shows the effective plastic strain distributions generated by the High-Fidelity Generalized Method of Cells which can be compared with the corresponding distributions generated by the finite-element model given in Fig. 16. As observed, both the magnitudes and the character of the distributions are virtually the same at the two strain levels. In particular, for the dilute case, initiation of yielding at the fiber/matrix interface at locations coincident with the loading axes is correctly captured by the high-fidelity model, as is the spread of the plastic zone at the final macroscopic strain. Yielding in the non-dilute case initiates halfway between adjacent fibers along the line rotated 45° about the fiber's center, in contrast with the dilute case. This too is captured by the high-fidelity model with excellent accuracy, as is the effective plastic strain distribution at the final macroscopic strain.

In order to highlight the differences between the High-Fidelity Generalized Method of Cells and the original Generalized Method of Cells, Fig. 17 illustrates the inplane shear stress σ_{23} distributions generated using the high-fidelity model at the same applied $\bar{\epsilon}_{33}$ strain levels as those presented in Fig 16. Clearly, the magnitude of the inplane shear stress is significant and cannot be neglected. The corresponding distributions obtained from the finite-element analysis are shown in Fig. 18. Comparison of the two sets of predictions reaffirms the predictive capability of the high-fidelity model. In stark contrast, the original Generalized

Method of Cells predicts that the inplane shear stress distributions are identically zero, which is a direct consequence of the absence of shear coupling. Apparently, the absence of shear coupling, while resulting in poor prediction of local distributions of certain stress components, has little effect on the method's ability to accurately capture the macroscopic behavior.

In order to explain the original Generalized Method of Cells' capability to capture the macroscopic response of metal matrix composites in the inelastic region with good accuracy, it is necessary to examine those stress distributions that are directly responsible for the inelastic behavior. In the case of the classical incremental plasticity theory employed herein, it is necessary to examine the effective stress distributions. These are illustrated in Figs. 19, 20, and 21 for the two fiber fraction cases generated at the same applied macroscopic strain levels as above using the High-Fidelity Generalized Method of Cells, finite-element analysis, and the original Generalized Method of Cells, respectively. Comparison of Figs. 19 and 20 leads to the same conclusions regarding the predictive capability of the high-fidelity model as the comparison of the effective plastic strain distributions shown in Figs. 15 and 16. Examination of the effective stress distributions generated using the original Generalized Method of Cells, Fig. 21, leads to the conclusion that the essential features of these distributions are generally the same as those obtained from the high-fidelity model and the finite-element analysis, Figs. 19 and 20, even though the local details differ somewhat. This explains the original Generalized method of Cells' ability to model the elastoplastic response of metal matrix composites with sufficient accuracy.

Finally, Figs. 22, 23, and 24 present the corresponding hydrostatic stress distributions generated using the High-Fidelity Generalized Method of Cells, finite-element analysis, and the original Generalized Method of Cells, respectively. As in the preceding cases, comparison of Figs. 22 and 23 indicates that the high-fidelity model captures both the magnitude and local distributions of the hydrostatic stress with very good accuracy relative to the finite-element predictions. In contrast, the accuracy with which these distributions are captured by the original Generalized Method of Cells is quite poor. It is only in a gross average sense that these distributions are accurate over large areas of the repeating unit cell, precluding the possibility of accurately modeling local matrix degradation or failure due to the hydrostatic stress component.

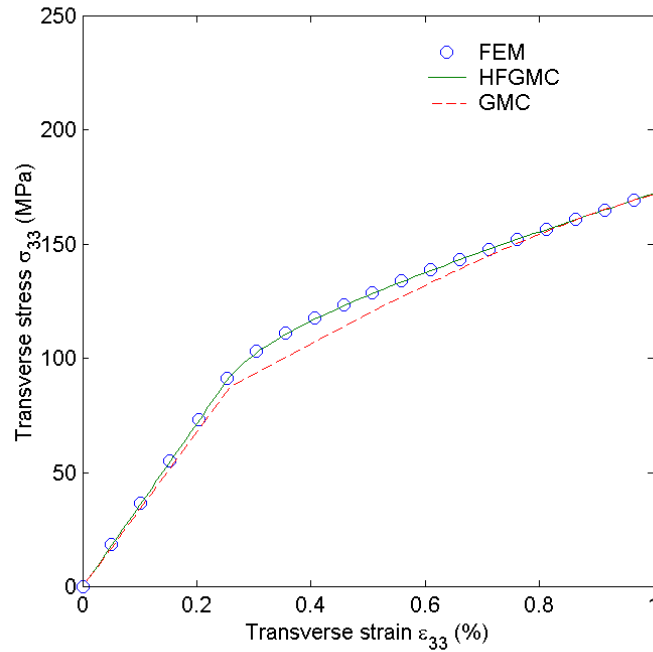
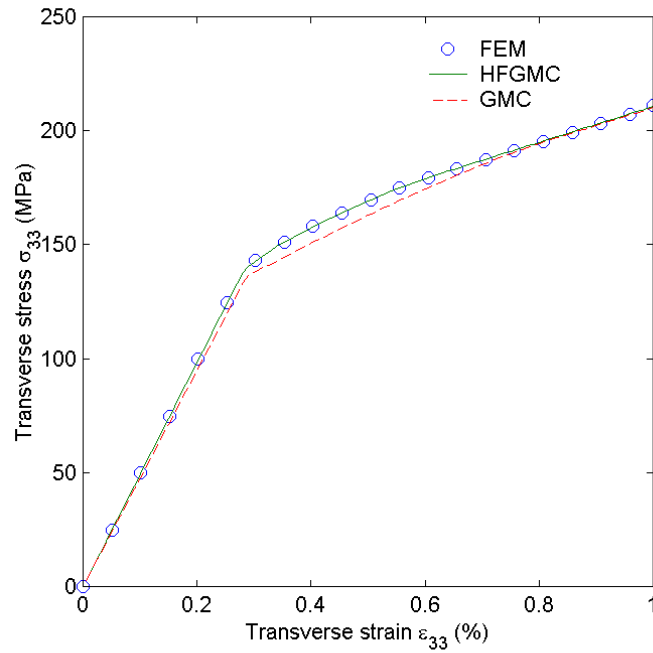


Figure 14. Macroscopic transverse stress-strain response, $\bar{\sigma}_{33}$ vs $\bar{\epsilon}_{33}$, of a unidirectional gr/al composite due to loading in the $x_2 - x_3$ plane by $\bar{\epsilon}_{22} = -\bar{\epsilon}_{33}$ with $\bar{\epsilon}_{11} = 0$: (top) $v_f = 0.05$; (bottom) $v_f = 0.25$. Comparison of the High-Fidelity Generalized Method of Cells predictions with the results from the finite-element analysis and the original General Method of Cells.

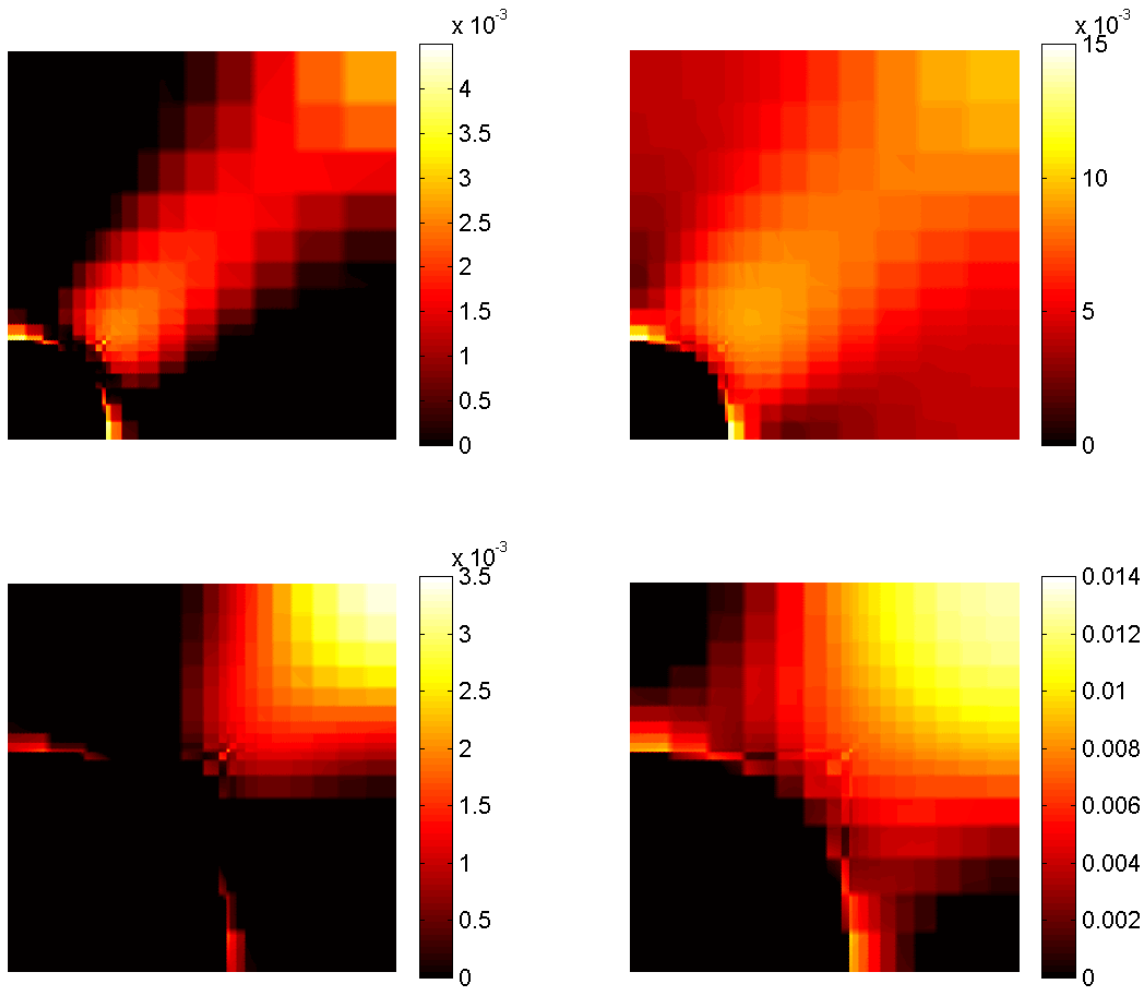


Figure 15. Effective plastic strain distributions in the aluminum phase of a unidirectional gr/al composite at the applied average transverse strain $\bar{\epsilon}_{33}$ of 0.4% (left column) and 1.0% (right column) obtained from the High-Fidelity Generalized Method of Cells: (top) $v_f = 0.05$; (bottom) $v_f = 0.25$.

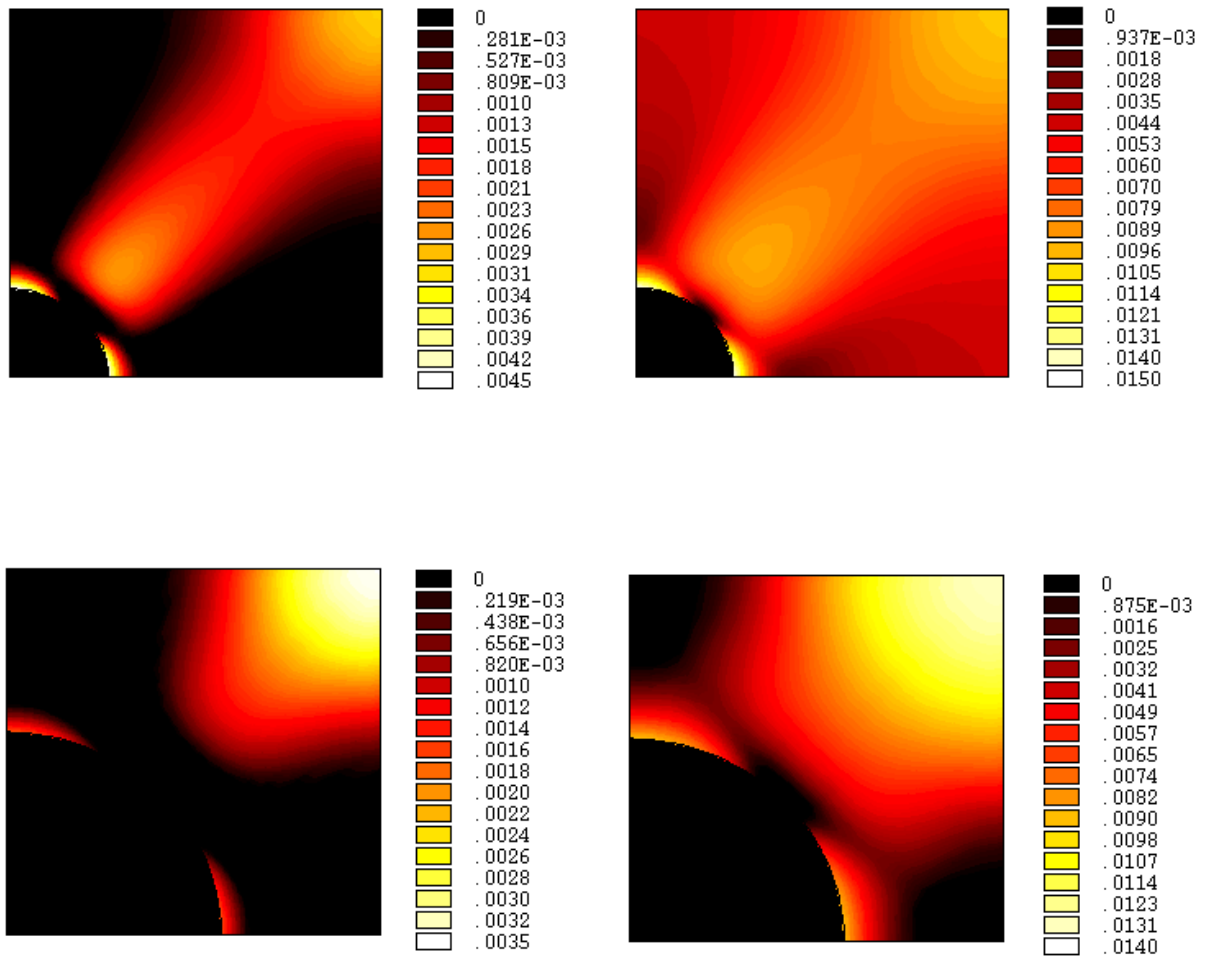


Figure 16. Effective plastic strain distributions in the aluminum phase a unidirectional gr/al composite at the applied average transverse strain $\bar{\epsilon}_{33}$ of 0.4% (left column) and 1.0% (right column) obtained from the finite-element analysis: (top) $v_f = 0.05$; (bottom) $v_f = 0.25$.

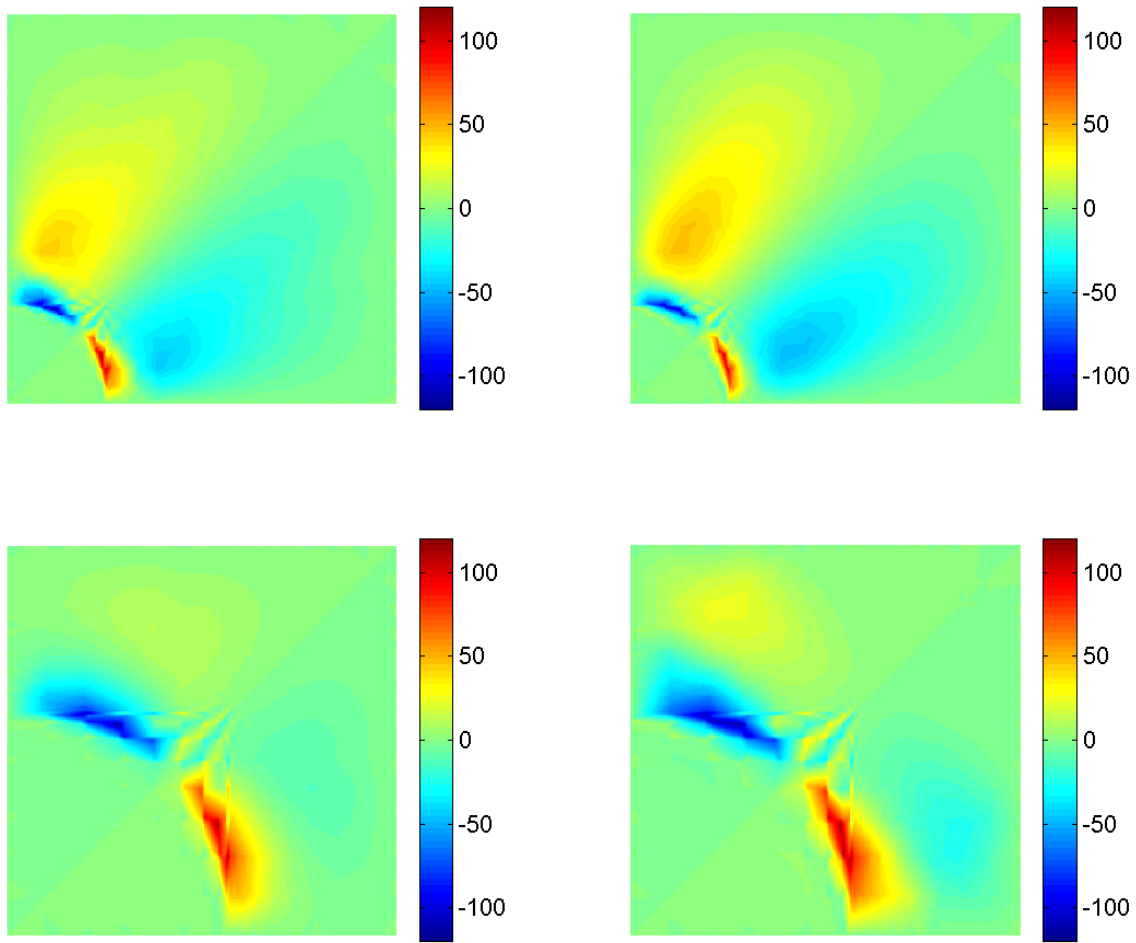


Figure 17. Inplane shear stress σ_{23} distributions in the individual phases a unidirectional gr/al composite at the applied average transverse strain $\bar{\epsilon}_{33}$ of 0.4% (left column) and 1.0% (right column) obtained from the High-Fidelity Generalized Method of Cells: (top) $v_f = 0.05$; (bottom) $v_f = 0.25$.

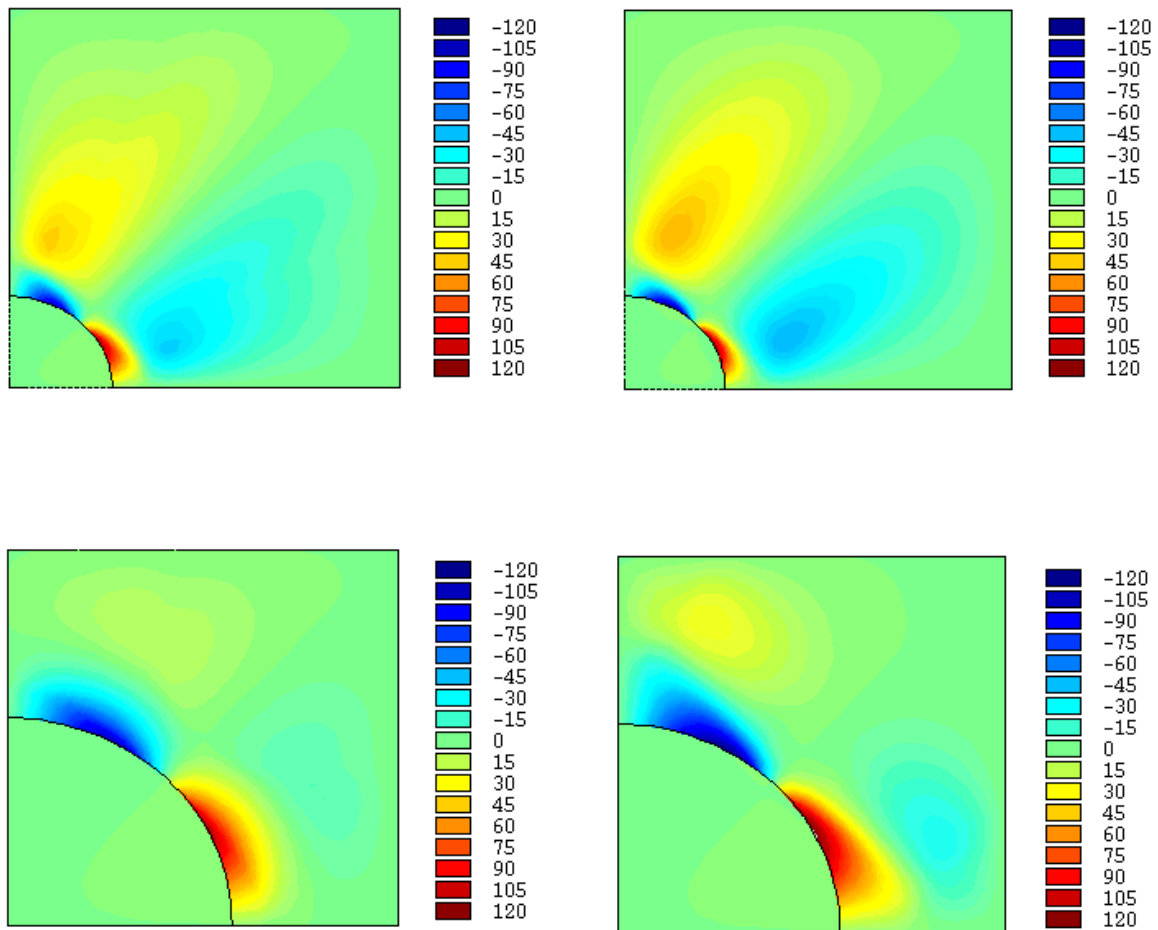


Figure 18. Inplane shear stress σ_{23} distributions in the individual phases a unidirectional gr/al composite at the applied average transverse strain $\bar{\epsilon}_{33}$ of 0.4% (left column) and 1.0% (right column) obtained from the finite-element analysis: (top) $v_f = 0.05$; (bottom) $v_f = 0.25$.

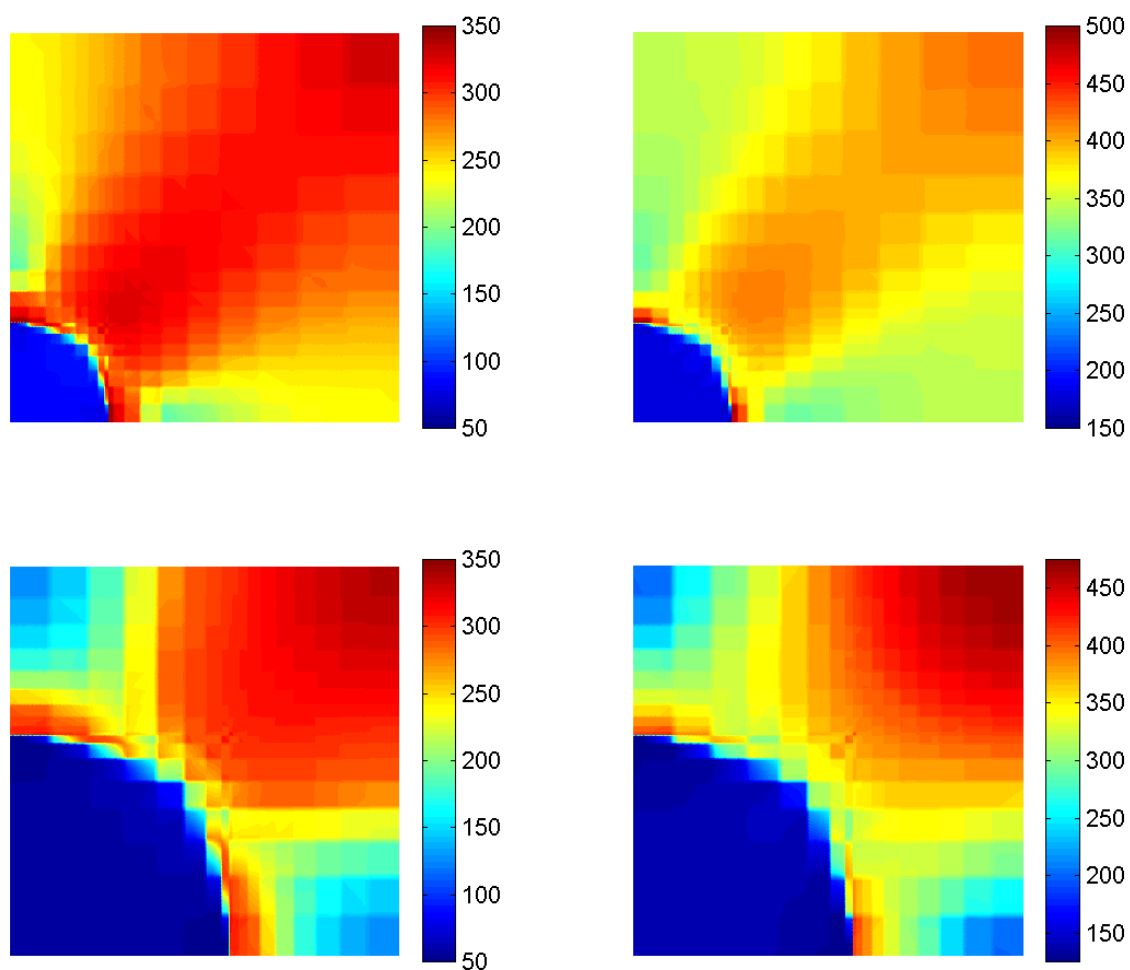


Figure 19. Effective stress distributions in the individual phases a unidirectional gr/al composite at the applied average transverse strain $\bar{\epsilon}_{33}$ of 0.4% (left column) and 1.0% (right column) obtained from the High-Fidelity Generalized Method of Cells: (top) $v_f = 0.05$; (bottom) $v_f = 0.25$.

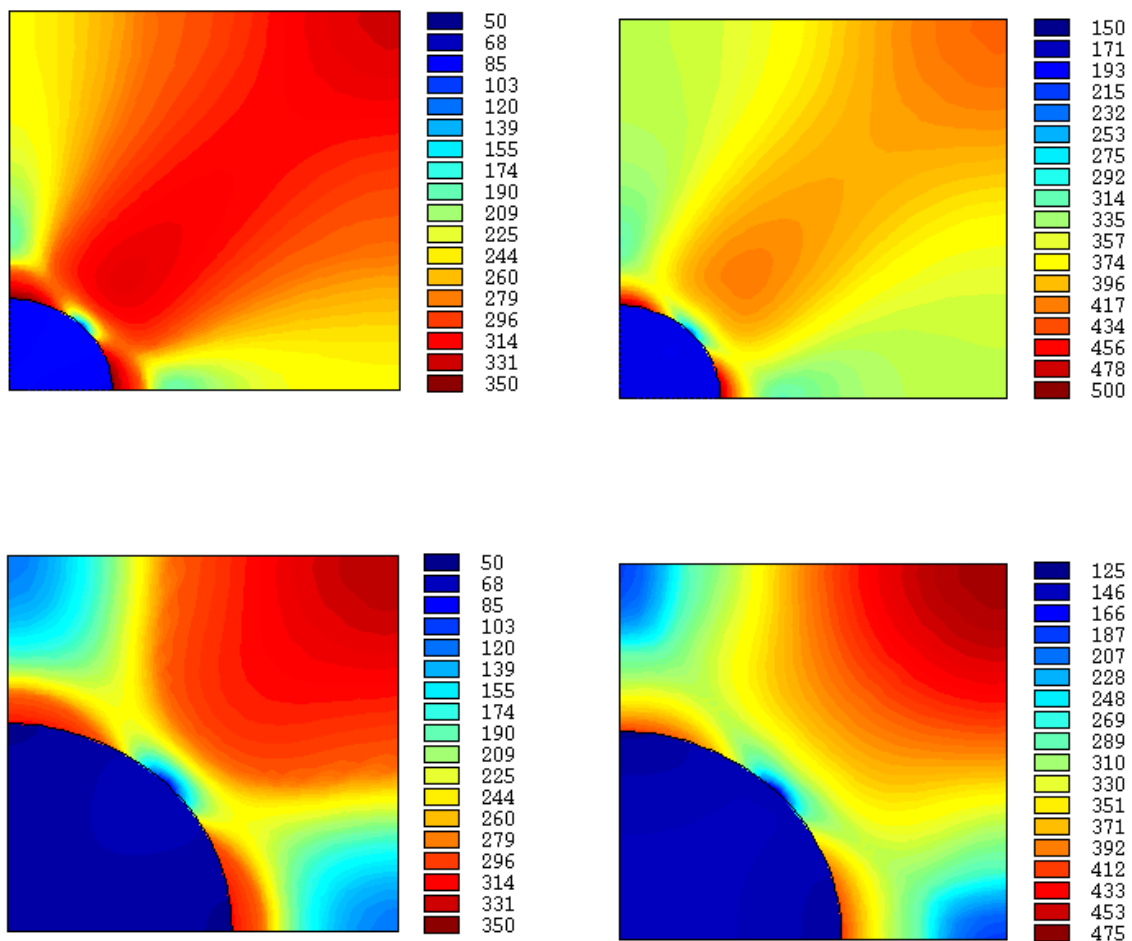


Figure 20. Effective stress distributions in the individual phases a unidirectional gr/al composite at the applied average transverse strain $\bar{\epsilon}_{33}$ of 0.4% (left column) and 1.0% (right column) obtained from the finite-element analysis: (top) $v_f = 0.05$; (bottom) $v_f = 0.25$.

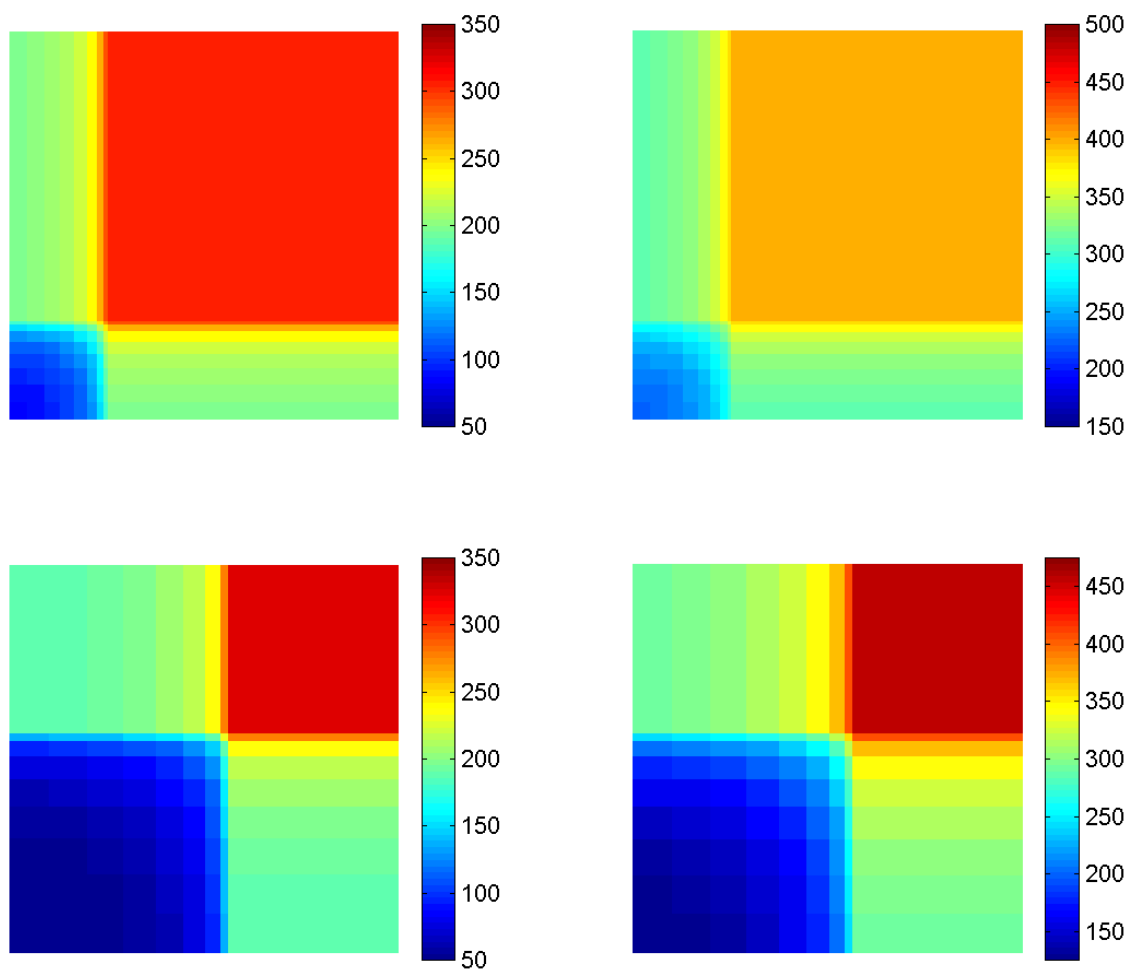


Figure 21. Effective stress distributions in the individual phases a unidirectional gr/al composite at the applied average transverse strain $\bar{\epsilon}_{33}$ of 0.4% (left column) and 1.0% (right column) obtained from the original Generalized Method of Cells: (top) $v_f = 0.05$; (bottom) $v_f = 0.25$.

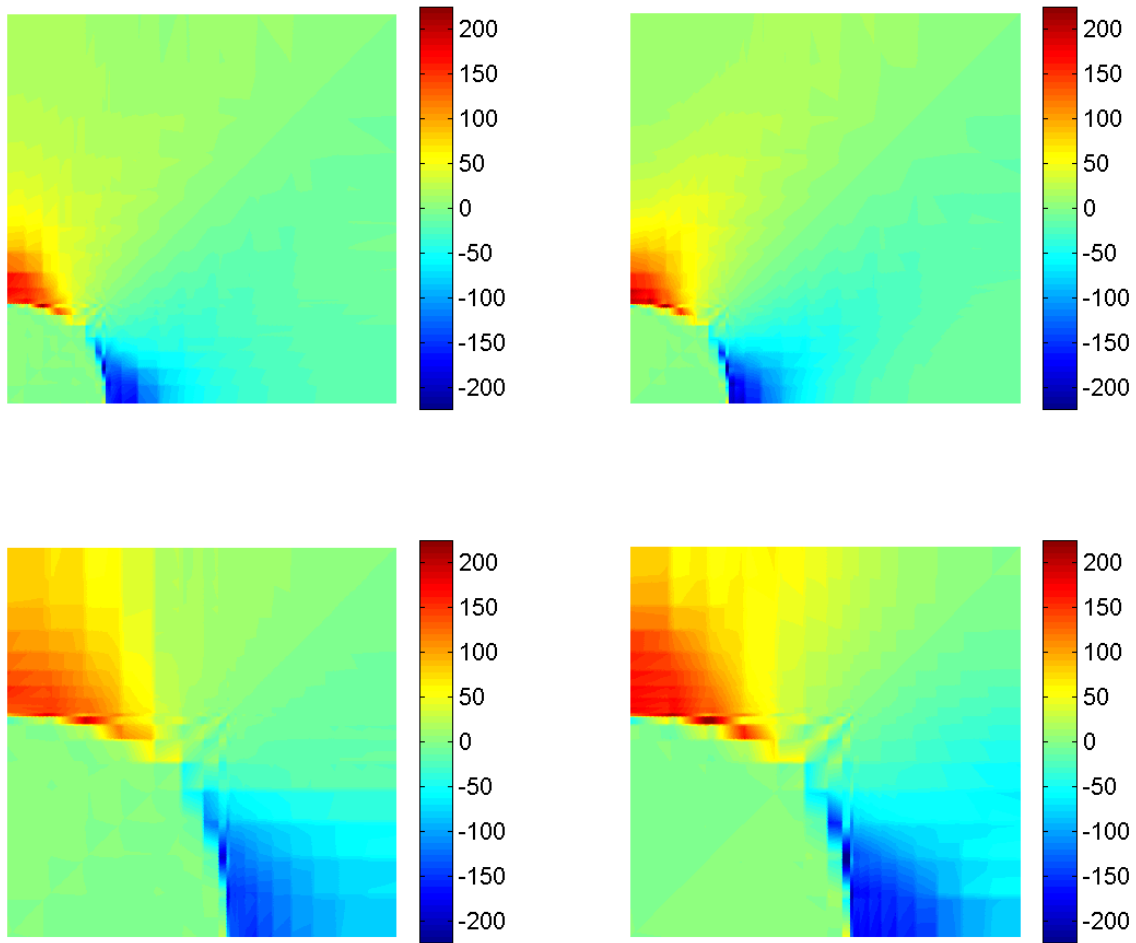


Figure 22. Hydrostatic stress distributions in the individual phases a unidirectional gr/al composite at the applied average transverse strain $\bar{\epsilon}_{33}$ of 0.4% (left column) and 1.0% (right column) obtained from the High-Fidelity Generalized Method of Cells: (top) $v_f = 0.05$; (bottom) $v_f = 0.25$.

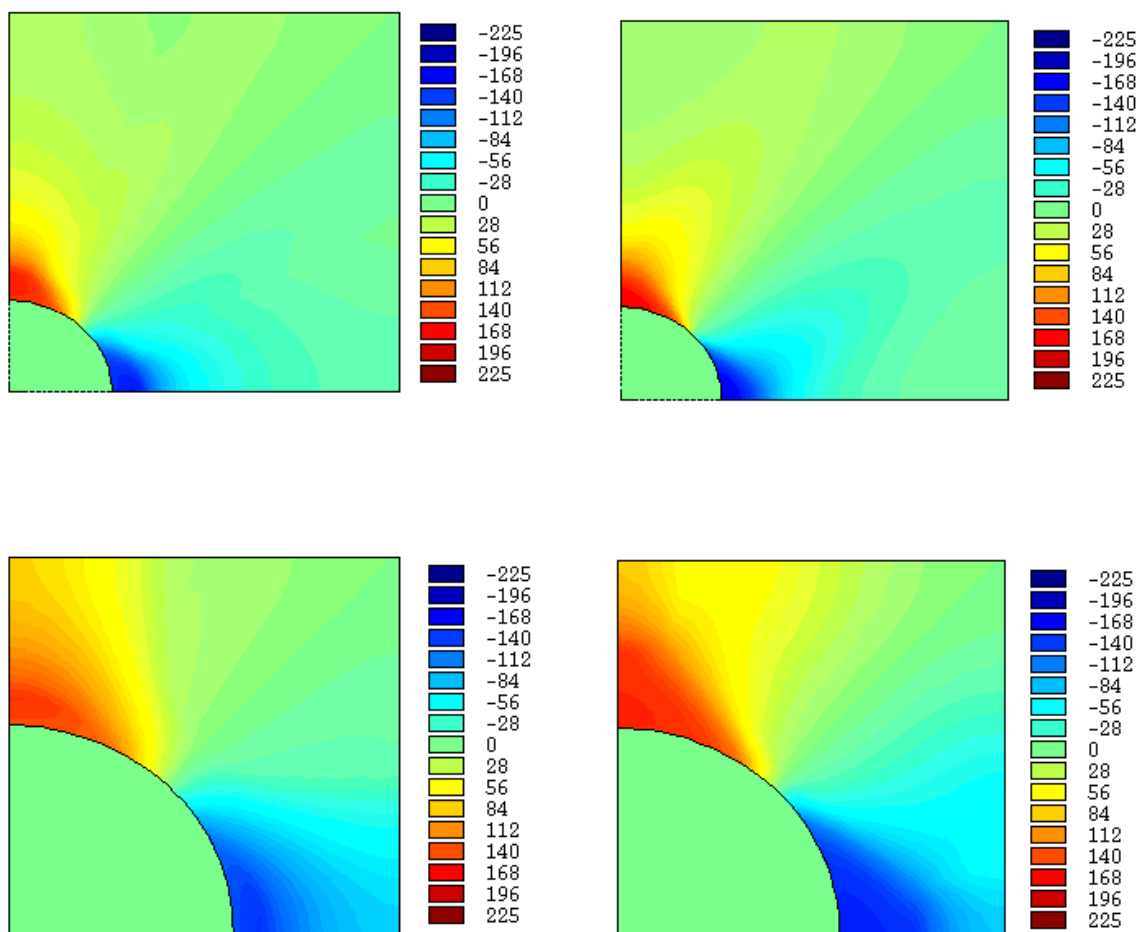


Figure 23. Hydrostatic stress distributions in the individual phases a unidirectional gr/al composite at the applied average transverse strain $\bar{\epsilon}_{33}$ of 0.4% (left column) and 1.0% (right column) obtained from the finite-element analysis: (top) $v_f = 0.05$; (bottom) $v_f = 0.25$.

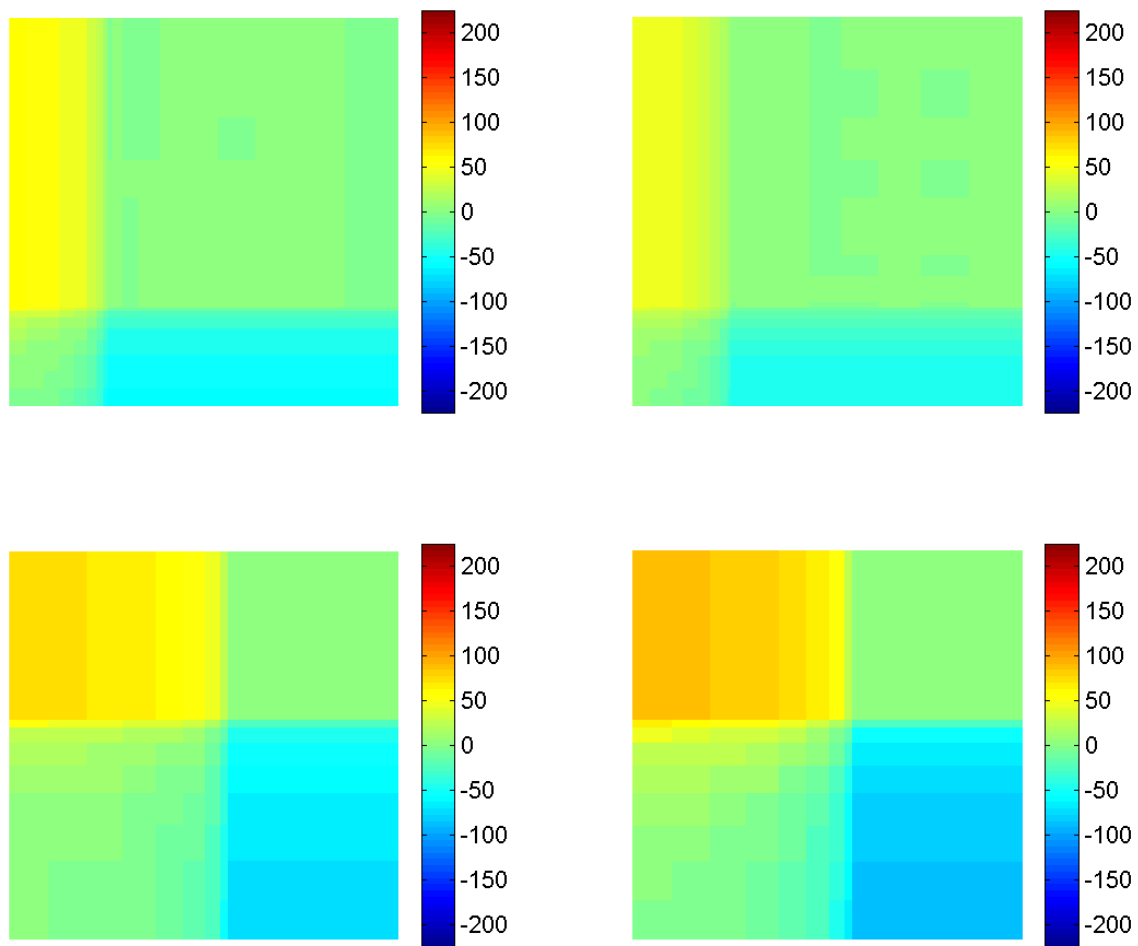


Figure 24. Hydrostatic stress distributions in the individual phases a unidirectional gr/al composite at the applied average transverse strain $\bar{\epsilon}_{33}$ of 0.4% (left column) and 1.0% (right column) obtained from the original Generalized Method of Cells: (top) $v_f = 0.05$; (bottom) $v_f = 0.25$.

4 Summary and Conclusions

A recently developed theory for periodic multiphase materials, called High-Fidelity Generalized Method of Cells, which was previously limited to thermoelastic phases has been extended herein to admit inelastic constitutive behavior of the individual phases. This extension has been carried out in a general fashion in order to enable the use of different constitutive models for the phase behavior, including classical incremental plasticity theory, creep models, as well as various unified viscoplasticity theories. The theoretical framework combines elements of the homogenization technique with the higher-order theory for functionally graded materials developed previously by the authors. These features provide a basis for consistent approximation of the displacement field at the local level together with consistent application of periodic boundary conditions imposed on the deformation of the repeating unit cell, which characterizes the material's microstructure. Further, the higher-order displacement field approximation at the local level employed in the present approach provides the necessary coupling between the local normal and inplane shear stress fields and the macroscopically applied loading. This coupling dramatically improves the accuracy of estimating the local stress and inelastic strain fields relative to the original Generalized Method of Cells which is based on a first-order displacement approximation at the local level. The high-fidelity model's predictive capability to capture both the macroscopic response and the local stress and inelastic strain fields has been demonstrated through comparison with the results of two analytical solutions and finite-element element analysis of the inelastic response of a unidirectional gr/al composite, based on the incremental plasticity theory, subjected to different types of loading.

The primary result of the High-Fidelity Generalized Method of Cells is the closed-form constitutive equation for the macroscopic thermoinelastic response of multiphase materials, subjected to arbitrary multiaxial macroscopic thermomechanical loading, which possess microstructures characterized by repeating unit cells with arbitrary reinforcement distributions. This is a direct result of the use of periodic boundary conditions that follow from the homogenization approach's framework. Thus the macroscopic inelastic response can be generated irrespective of whether or not a repeating unit cell possesses planes of material symmetry. This can be done easily for any combination of macroscopically applied thermomechanical loads, in contrast with the standard finite-element analyses of periodic composites. The repeating unit cell's construction is simple due to the employed volume discretization that produces a rectangular grid whose subcells are appropriately assigned different material properties and dimensions so as to mimic a multiphase material's actual microstructure. Further, the computational speed with which the macroscopic inelastic response and local stress and plastic strain fields are generated is sufficiently fast (typically on the order of a few minutes on the DEC-Alpha DS20E 6/667 machine for the investigated cases) for reasonably detailed volume discretizations of a repeating unit cell. These features of the presented theory facilitate investigations of the impact of different materials architectures on both the macroscopic and local responses, taking into account inelastic phase behavior, in an efficient and accurate manner. They also make it straightforward to incorporate the theory into a structural analysis computer code as a subroutine.

References

- Aboudi, J., 1982. A continuum theory for fiber-reinforced elastic-viscoplastic composites, *Int. J. Engineering Science*, 20, 605-621.
- Aboudi, J., 1996. Micromechanical analysis of composites by the method of cells - update, *Applied Mechanics Reviews*, 49(10), (Part 2), S83-S91.
- Aboudi, J., Pindera, M-J., and Arnold, S. M., 1996. Thermoelastic theory for the response of materials functionally graded in two directions, *Int. J. Solids & Structures*, 33(7), 931-966.
- Aboudi, J., Pindera, M-J., and Arnold, S. M., 1999. Higher-order theory for functionally graded materials, *Composites: Part B (Engineering)*, 30(8), 777-832.
- Aboudi, J., Pindera, M-J., and Arnold, S. M., 2001. Linear thermoelastic higher-order theory for periodic multiphase materials, *J. Applied Mechanics*, 68(5), 697-707.
- Arnold, S. M., Pindera, M-J., and Wilt, T. E., 1996. Influence of fiber architecture on the inelastic response of metal matrix composites, *Int. J. Plasticity*, 12(4), 507-545.
- Bednarczyk, B. A. and Arnold, S. M., 2001a. Micromechanics-based deformation and failure prediction for longitudinally reinforced titanium matrix composites, *Composites Science and Technology*, 61, 705-729.
- Bednarczyk, B. A. and Arnold, S. M., 2001b. Transverse tensile and creep modeling of continuously reinforced titanium composites with local debonding, *Int. J. Solids & Structures* (in press).
- Chaboche, J. L., Kruch, S., Maire, J. F., and Pottier, J., 2001. Towards a micromechanics based inelastic and damage modeling of composites, *Int. J. Plasticity*, 17, 411-439.
- Dvorak, G. J., 1992. Transformation field analysis of inelastic composite materials, *Proc. Royal Society of London*, A431, 89-110.
- Dvorak, G. J., 2000. Composite materials: inelastic behavior, damage, fatigue and fracture, *In. J. Solids & Structures*, 37, 155-170.
- Fotiu, P. A. and Nemat-Nasser, S., 1996. Overall properties of elastic-viscoplastic periodic composites, *Int. J. Plasticity*, 12(2), 163-190.
- Hill, R., 1963. Elastic properties of reinforced solids: some theoretical principles, *J. Mech. Phys. Solids*, 11, 357-372.
- Kalamkarov, A. L. and Kolpakov, A. G., 1997. *Analysis, Design and Optimization of Composite Structures*, John Wiley & Sons, New York.
- Levin, V. M., 1967. On the coefficients of thermal expansion of heterogeneous materials, *Mekh, Tverd. Tela* (in Russian), 1, p. 88. (see also: *Mech. Solids*, 2, 88-94, 1967, English transl.).
- Mendelson, A., 1986. *Plasticity: Theory and Application*, Krieger Publishing Co., Malabar, FL (reprint edition).
- Pahr, D. H. and Arnold, S. M., 2001. The applicability of the generalized method of cells for analyzing discontinuously reinforced composites, NASA/TM-2001-211165, NASA-Glenn Research Center, Cleveland, OH.
- Paley, M. and Aboudi, J., 1992. Micromechanical analysis of composites by the generalized method of cells, *Mechanics of Materials*, 14, 127-139.
- Parton, V. Z. and Kudryavtsev, B. A., 1993. *Engineering Mechanics of Composite Structures*, CRC Press, Boca Raton, FL.
- Pindera, M-J., Freed, A. D., and Arnold, S. M., 1993. Effects of fiber and interfacial layer morphologies on the thermoplastic response of metal matrix composites, *Int. J. Solids & Structures*, 30(9), 1213-1238.

- Pindera, M-J. and Bednarczyk, B. A., 1999. An efficient implementation of the generalized method of cells for unidirectional, multi-phased composites with complex microstructures, *Composites: Part B (Engineering)*, 30(1), 87-105.
- Sanchez-Palencia, E., 1980. Non-homogeneous media and vibration theory, *Lecture Notes in Physics*, 127, Springer-Verlag, Berlin (New York).
- Sun, C. T. and Vaidya, R. S., 1996. Prediction of composite properties from a representative volume element, *Composites Science and Technology*, 56, 171-179.
- Suquet, P. M., 1987. Elements of homogenization for inelastic solid mechanics, *Lecture Notes in Physics*, 272, pp. 193-278. Springer-Verlag, Berlin (New York).
- Walker, K. P., Freed, A. D., and Jordan, E. H., 1994. Thermoviscoplastic analysis of fibrous periodic composites by the use of triangular subvolumes, *Composites Science and Technology*, 50(1), 71-84.
- Williams, T. O. and Pindera, M-J., 1997. An analytical model for the inelastic axial shear response of unidirectional metal matrix composites, *Int. J. Plasticity*, 13(3), 261-289.

Appendix: Multiple Concentric Cylinder Model

A brief outline of the solutions for the displacement field, from which the corresponding stress field can be generated, in a unidirectional elastoplastic composite subjected to axisymmetric and axial shear loading is given in this section based on the multiple concentric cylinder model. The solutions are fully analytical and therefore provide a good basis for comparison with the predictions of the outlined higher-order theory despite the differences in the model geometries. The cylindrical coordinate system $x-r-\theta$ (where x denotes the direction along the cylinder's axis) is used to formulate the problem and solve for the displacement and stress fields in a multilayered cylinder consisting of an elastic core and an arbitrary number of fully bonded inelastic concentric shells. The elastic core is denoted by the superscript 1 and the outermost cylindrical shell by n . The inner radius of the k th shell is denoted by r_{k-1} and the outer radius by r_k .

Axisymmetric loading

Under axisymmetric loading that may involve a combination of a macroscopically uniform axial stress or strain, uniform temperature field and biaxial tension/compression, the displacement field in the individual layers of a multiple concentric cylinder has the following form

$$u_x = \varepsilon_{xx}^0 x, \quad u_r = u_r(r), \quad u_\theta = 0 \quad (\text{A1})$$

where ε_{xx}^0 is the uniform axial strain component. Therefore, the equilibrium equations in the individual layers expressed in terms of displacements reduce to the single ordinary differential equation

$$\frac{d^2 u_r}{dr^2} + \frac{1}{r} \frac{du_r}{dr} - \frac{u_r}{r^2} = \frac{1}{r} \sum_{i=x,\theta,r} \frac{(C_{ri} - C_{\theta i})}{C_{rr}} \varepsilon_{ii}^{in}(r) + \sum_{i=x,\theta,r} \frac{C_{ri}}{C_{rr}} \frac{d\varepsilon_{ii}^{in}(r)}{dr} \quad (\text{A2})$$

where $\varepsilon_{ii}^{in}(r)$ are the inelastic strain distributions that depend implicitly on the radial displacement field $u_r(r)$, and C_{ij} ($i, j = x, \theta, r$) terms are the components of the elastic stiffness matrix expressed in the cylindrical coordinate system. For the elastic core, the right hand side of the above equation becomes zero. In the present situation, we consider thermal loading due to a spatially uniform temperature change. Therefore, the solution to the above equation in each layer of the composite cylinder is obtained subject to the boundary conditions

$$\sigma_{rr}^n(r_n) = 0, \quad (\text{A3})$$

the interfacial displacement and traction continuity conditions

$$u_r^{k-1}(r_{k-1}) = u_r^k(r_{k-1}), \quad \sigma_{rr}^{k-1}(r_{k-1}) = \sigma_{rr}^k(r_{k-1}) \quad (\text{A4})$$

where $k = 2, \dots, n$, and the axial equilibrium condition for the entire multiple concentric cylinder assemblage

$$\int_{A_c} \sigma_{xx} dA_c = 0 \quad (\text{A5})$$

where A_c is the cross-sectional area of the assemblage.

Using standard techniques, the solution of the equilibrium equation in each layer is obtained in the form

$$\begin{aligned} u_r(r) = & A_1 r + \frac{A_2}{r} + \frac{1}{2r} \int_{r_{k-1}}^r \sum_{i=x,\theta,r} \frac{(C_{ri} + C_{\theta i})}{C_{rr}} \varepsilon_{ii}^{in}(r') r' dr' + \\ & \frac{r}{2} \int_{r_{k-1}}^r \sum_{i=x,\theta,r} \frac{(C_{ri} - C_{\theta i})}{C_{rr}} \varepsilon_{ii}^{in}(r') \frac{dr'}{r'} + \frac{1}{2} \sum_{i=x,\theta,r} \frac{C_{ri}}{C_{rr}} \varepsilon_{ii}^{in}(r_{k-1}) r \left(\frac{r_{k-1}^2}{r^2} - 1 \right) \end{aligned} \quad (\text{A6})$$

where $r_{k-1} \leq r \leq r_k$. The unknown coefficients A_1, A_2 , axial strain ε_{xx}^0 , and inelastic strain distributions in the core and the k th shell are obtained at each increment along the imposed thermal loading path by following the solution procedure outlined by Pindera *et al.* (1993). The imposed spatially uniform thermal loading appears in the solution procedure through the application of the interfacial traction continuity and external boundary conditions upon expressing tractions in terms of strains (and thus the displacement field) using Hooke's law.

Axial shear loading

Under axial shear loading by homogeneous displacements or tractions that produce a uniform axial shear strain in an equivalent homogenized medium, the displacement field takes the following form, referred to the coordinate system of Fig. A1,

$$u_x(r, \theta) = \phi(r, \theta) - \varepsilon_{12}^0 r \cos \theta, \quad u_r(x, \theta) = \varepsilon_{12}^0 x \cos \theta, \quad u_\theta(x, \theta) = -\varepsilon_{12}^0 x \sin \theta \quad (\text{A7})$$

where ε_{12}^0 is the uniform shear strain in an equivalent homogenized medium generated by homogeneous displacement or traction boundary conditions in the horizontal plane. The function $\phi(r, \theta)$ represents the deviation in the axial shear deformation of a layer from the solution for the equivalent homogenized material with homogeneous properties and, in the presence of inelastic effects, depends implicitly on the inelastic strain field. Therefore, the equilibrium equations in the individual layers expressed in terms of displacements result in the following partial differential equation for the unknown function $\phi(r, \theta)$ in each layer

$$\frac{1}{r} \frac{\partial}{\partial r} \left(r \frac{\partial \phi}{\partial r} \right) + \frac{1}{r^2} \frac{\partial^2 \phi}{\partial \theta^2} = \frac{1}{r} \frac{\partial (r \varepsilon_{xr}^{in})}{\partial r} + \frac{1}{r} \frac{\partial \varepsilon_{x\theta}^{in}}{\partial \theta} \equiv e(r, \theta) \quad (\text{A8})$$

The solution to the above equation is obtained subject to the homogeneous displacement boundary conditions imposed on the surface of the n th shell

$$u_x(r, \theta) = \varepsilon_{12}^0 b \cos \theta, \quad u_r(x, \theta) = \varepsilon_{12}^0 x \cos \theta, \quad u_\theta(x, \theta) = -\varepsilon_{12}^0 x \sin \theta \quad (\text{A9})$$

where b is the outer radius of the entire cylindrical assemblage, and the interfacial displacement and traction continuity conditions. For the above displacement field representation, these reduce to

$$u_x^{k-1}(r_{k-1}, \theta) = u_x^k(r_{k-1}, \theta), \quad \sigma_{xr}^{k-1}(r_{k-1}, \theta) = \sigma_{xr}^k(r_{k-1}, \theta) \quad (\text{A10})$$

since the continuity of the radial and tangential displacement components $u_r(x, \theta)$ and $u_\theta(x, \theta)$ is identically satisfied, and the traction components σ_{rr} and $\sigma_{r\theta}$ vanish.

The solution to the partial differential equation governing the function $\phi(r, \theta)$ is obtained in the form

$$\phi(r, \theta) = \frac{1}{\sqrt{2\pi}} R_0(r) + \frac{1}{\sqrt{\pi}} \sum_{n=1}^{\infty} R_n(r) \cos n\theta \quad (\text{A11})$$

where

$$R_0(r) = [F_{10} + \int_{r_{k-1}}^r s f_0(s) ds] \ln r + F_{20} - \int_{r_{k-1}}^r s \ln s f_0(s) \quad (\text{A12})$$

for $n = 0$, and

$$R_n(r) = [F_{1n} + \frac{1}{2n} \int_{r_{k-1}}^r s^{-n+1} f_n(s) ds] r^n + [F_{2n} - \frac{1}{2n} \int_{r_{k-1}}^r s^{n+1} f_n(s) ds] r^{-n} \quad (\text{A13})$$

for $n > 0$. The functions $f_n(r)$ are the coefficients of the Fourier series representation of $e(r, \theta)$. They are given by

$$f_n(r) = \frac{1}{\sqrt{\pi}} \int_{-\pi}^{\pi} e(r, \theta) \cos n\theta d\theta \quad (\text{A14})$$

The unknown coefficients F_{1n} and F_{2n} appearing in the solution for $\phi(r, \theta)$ in each layer are obtained by applying the interfacial displacement and traction continuity conditions, external boundary conditions, and employing an iterative solution procedure at each load increment in the manner described by Williams and Pindera (1997). Convergent solutions in the presence of inelastic effects are typically obtained with 25 – 30 harmonics in the Fourier series representation of $\phi(r, \theta)$.

EQUIVALENT HOMOGENIZED MEDIUM

**Displacement bc's for
homogeneous shearing
in the x_1 - x_2 plane**

$$u_1 = \varepsilon_{12}^o x_2$$

$$u_2 = \varepsilon_{12}^o x_1$$

$$u_3 = 0$$

**Corresponding
displacement bc's
on the lateral surface
of a homogenized
cylinder**

$$u_x = \varepsilon_{12}^o b \cos \theta$$

$$u_r = \varepsilon_{12}^o x \cos \theta$$

$$u_\theta = \varepsilon_{12}^o x \sin \theta$$

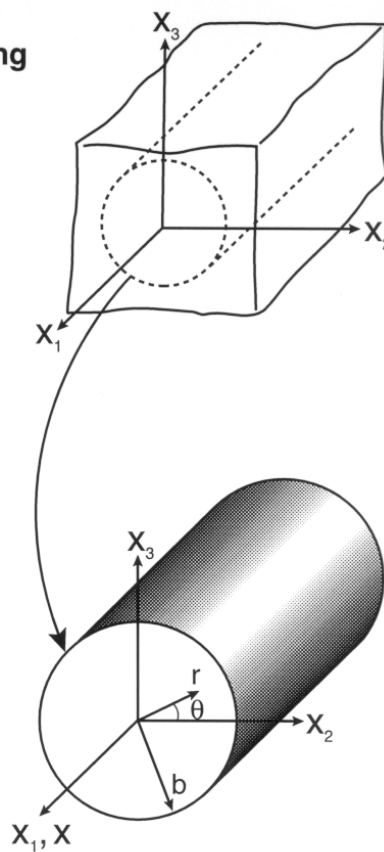


Figure A1. Boundary conditions for the multiple concentric cylinder model subjected to axial shearing in the $x_1 - x_2$ plane.

REPORT DOCUMENTATION PAGE			Form Approved OMB No. 0704-0188	
Public reporting burden for this collection of information is estimated to average 1 hour per response, including the time for reviewing instructions, searching existing data sources, gathering and maintaining the data needed, and completing and reviewing the collection of information. Send comments regarding this burden estimate or any other aspect of this collection of information, including suggestions for reducing this burden, to Washington Headquarters Services, Directorate for Information Operations and Reports, 1215 Jefferson Davis Highway, Suite 1204, Arlington, VA 22202-4302, and to the Office of Management and Budget, Paperwork Reduction Project (0704-0188), Washington, DC 20503.				
1. AGENCY USE ONLY (Leave blank)		2. REPORT DATE March 2002		3. REPORT TYPE AND DATES COVERED Technical Memorandum
4. TITLE AND SUBTITLE High-Fidelity Generalization Method of Cells for Inelastic Periodic Multiphase Materials			5. FUNDING NUMBERS WU-708-73-35-00	
6. AUTHOR(S) Jacob Aboudi, Marek-Jerzy Pindera, and Steven M. Arnold				
7. PERFORMING ORGANIZATION NAME(S) AND ADDRESS(ES) National Aeronautics and Space Administration John H. Glenn Research Center at Lewis Field Cleveland, Ohio 44135-3191			8. PERFORMING ORGANIZATION REPORT NUMBER E-13234	
9. SPONSORING/MONITORING AGENCY NAME(S) AND ADDRESS(ES) National Aeronautics and Space Administration Washington, DC 20546-0001			10. SPONSORING/MONITORING AGENCY REPORT NUMBER NASA TM-2002-211469	
11. SUPPLEMENTARY NOTES Jacob Aboudi, Tel-Aviv University, Ramat-Aviv 69978, Israel; Marek-Jerzy Pindera, University of Virginia, Charlottesville, Virginia 22903; and Steven M. Arnold, NASA Glenn Research Center. Responsible person, S.M. Arnold, organization code 5920, 216-433-3334.				
12a. DISTRIBUTION/AVAILABILITY STATEMENT Unclassified - Unlimited Subject Categories: 24 and 39 Available electronically at http://gltrs.grc.nasa.gov/GLTRS This publication is available from the NASA Center for AeroSpace Information, 301-621-0390.			12b. DISTRIBUTION CODE	
13. ABSTRACT (Maximum 200 words) An extension of a recently-developed linear thermoelastic theory for multiphase periodic materials is presented which admits inelastic behavior of the constituent phases. The extended theory is capable of accurately estimating both the effective inelastic response of a periodic multiphase composite and the local stress and strain fields in the individual phases. The model is presently limited to materials characterized by constituent phases that are continuous in one direction, but arbitrarily distributed within the repeating unit cell which characterizes the material's periodic microstructure. The model's analytical framework is based on the homogenization technique for periodic media, but the method of solution for the local displacement and stress fields borrows concepts previously employed by the authors in constructing the higher-order theory for functionally graded materials, in contrast with the standard finite-element solution method typically used in conjunction with the homogenization technique. The present approach produces a closed-form macroscopic constitutive equation for a periodic multiphase material valid for both uniaxial and multiaxial loading. The model's predictive accuracy in generating both the effective inelastic stress-strain response and the local stress said inelastic strain fields is demonstrated by comparison with the results of an analytical inelastic solution for the axisymmetric and axial shear response of a unidirectional composite based on the concentric cylinder model, and with finite-element results for transverse loading.				
14. SUBJECT TERMS Micromechanics; Elastic; Plastic; Deformation; Composites			15. NUMBER OF PAGES 55	
			16. PRICE CODE	
17. SECURITY CLASSIFICATION OF REPORT Unclassified	18. SECURITY CLASSIFICATION OF THIS PAGE Unclassified	19. SECURITY CLASSIFICATION OF ABSTRACT Unclassified	20. LIMITATION OF ABSTRACT	